Nonlinear Analysis: Hybrid Systems 52 (2024) 101469

Contents lists available at ScienceDirect

Nonlinear Analysis: Hybrid Systems

journal homepage: www.elsevier.com/locate/nahs

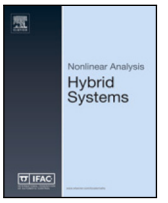

A nonsmooth RATTLE algorithm for mechanical systems with frictional unilateral constraints

Jonas Breuling [a,*], Giuseppe Capobianco [b], Simon R. Eugster [a], Remco I. Leine [a]

[a] Institute for Nonlinear Mechanics, University of Stuttgart, Pfaffenwaldring 9, Stuttgart, 70569, Germany
[b] Institute of Applied Dynamics, Friedrich-Alexander-Universität Erlangen-Nürnberg, Immerwahrstrasse 1, Erlangen, 91058, Germany

ARTICLE INFO

Keywords:
Nonsmooth contact dynamics
Higher-order
Unilateral constraints
Coulomb friction

ABSTRACT

In 1983, Andersen proposed the RATTLE algorithm as an extension of the SHAKE algorithm. The RATTLE algorithm is a well-established method for simulating mechanical systems with perfect bilateral constraints. This paper further extends RATTLE for simulating nonsmooth mechanical systems with frictional unilateral constraints (i.e. frictional contact). With that, it satisfies the need for higher-order integration methods within the framework of nonsmooth contact dynamics in phases where the contact status does not change (i.e. no collisions/constant sliding states). In particular, the proposed method can simulate impact-free motions, such as persistent frictional contact, with second-order accurate positions and velocities and prohibits penetration by unilateral constraints on position level.

1. Introduction

Nonsmooth mechanics has emerged as a significant branch of mechanics that deals with systems that exhibit discontinuous behavior such as collisions, impacts, and friction, see e.g. [1–5]. It has proven to be an effective tool for analyzing the dynamics of complex systems in various applications, from mechanical engineering [6] to natural hazard research [7]. Time-integration methods for nonsmooth mechanics are classically distinguished as either being event-driven [4] or as being event-capturing [1–3,5] methods. Since the former is mainly designed for systems with a small number of events and cannot describe accumulation points, we focus on the latter approach.

For applications without elastic impacts, a popular event-capturing method for the simulation of mechanical systems subjected to frictional unilateral constraints was proposed by [8]. When also elastic impacts should be included, two major methods have been established. The first method, known as the Moreau–Jean method [1,9–11], solves the constraints at the velocity level while incorporating a Newton-type impact law. The second method, referred to as the Schatzman–Paoli method [12,13], directly considers the constraints at the position level and is restricted to frictionless unilateral constraints. Various variants of these methods have also been proposed and extensively discussed in literature (see e.g. [3] for further information). However, any of these methods is convergent of order one, even on time intervals without collisions, i.e., the total error decreases linearly with step-size [3]. Using such first-order methods, the numerical solution of nonsmooth mechanical systems with friction requires demanding restrictions on the step-size choice in order to solve the underlying equations with satisfactory accuracy. Higher-order integration methods are therefore a welcome alternative.

Up to now, there is no straightforward extension of higher-order integration methods to nonsmooth mechanical systems. Nonetheless, a few attempts were made. For frictionless contacts, applicability of extrapolation methods are discussed in [14],

* Corresponding author.
E-mail address: jonas.breuling@inm.uni-stuttgart.de (J. Breuling).

https://doi.org/10.1016/j.nahs.2024.101469
Received 29 June 2023; Received in revised form 5 October 2023; Accepted 28 January 2024
Available online 6 February 2024

while in [15] higher-order event-capturing methods are designed by coupling implicit Runge–Kutta methods with Moreau's time-stepping method. Using mollifier functions, Clenshaw–Curtis quadrature rules and an appropriate impact representation, application of discontinuous Galerkin methods resulted in two Runge–Kutta collocation families [16] with higher-order accuracy during non-impulsive phases. Further, their algorithms cope with frictional contacts. A nonsmooth extension of the classical generalized-alpha method, a sophisticated algorithm for solving smooth structural dynamics problems, was presented in [17]. However, all mentioned higher-order methods have in common that the unilateral constraints (including Newton-type impact laws) are formulated on velocity level. Hence, penetration is not prohibited by these methods which is a serious problem in scenarios where the contact geometry changes rapidly, see Example 10.3 of [18].

A remedy for the nonphysical penetration behavior is given by the simultaneous enforcement of unilateral constraints at position and velocity levels using a nonsmooth generalized-alpha method [19]. More generally, the authors applied a stabilization of the constraint drift in the sense of Gear–Gupta–Leimkuhler (GGL) [20], see also [21,22]. Based on these investigations, a variety of derivatives of the original nonsmooth generalized-alpha method [17] were developed, e.g. [23,24]. Specifically, in [18,25,26], these methods have been extended to cope with frictional contact and a more general kinematic relation between generalized positions and velocities. On the one hand, these algorithms require the evaluation of the constraint accelerations of both unilateral and bilateral constraints or use a decoupled (simplified) solution of the underlying equations. The former one requires an elaborate active-set strategy for the solution of the arising nonlinear system of equations. Moreover, cumbersome Jacobians of the constraints, as well as the constraint velocities and accelerations are required. The latter one simplifies the underlying mechanics which results in first-order convergence during persistent friction [25]. Hence, these methods are not DAE-consistent, i.e., for persistent frictional contact, which can be described by differential algebraic equations (DAE), these methods do not collapse to a higher-order DAE algorithm.

Structure preserving algorithms are investigated in different areas of research as astronomy, molecular dynamics, mechanics and theoretical physics. It turned out that they produce improved qualitative results and allow for more accurate long-time integration compared to other general-purpose methods [27]. Hence, we are interested in the extension of such methods to the class of nonsmooth mechanical systems with frictional unilateral constraints. Based on the Störmer–Verlet method, the most simplest second-order accurate algorithm for the solution of mechanical systems subjected to holonomic bilateral constraints is called SHAKE [28]. Unfortunately, the involved three-term recursion may lead to round-off errors. Hence, a reformulation as a single-step method is advisable. This is called the velocity-Verlet method [27]. It consists of two consecutive velocity updates and does not require to store the positions of the penultimate step. Its direct application to the SHAKE algorithm is not possible, since the Lagrange multipliers from the current and future time step would be required. Obviously, the future value is not known during the current iteration unless all time steps are solved monolithically. As a remedy, Andersen [29] in 1983 proposed to also satisfy the time derivatives of the bilateral constraints by replacing the future Lagrange multiplier with an additional independent one. Hence, the numerical solution satisfies the constraint conditions as well as their time derivatives and the found solution lies exactly on the constraint manifold of the system. The resulting algorithm is called RATTLE [29].

As noted later [27], the velocity-Verlet method (also called leapfrog) can be applied to general partitioned differential equations and can be interpreted as a partitioned Runge–Kutta method with the following Butcher tableaus:

0	0	0
1	1/2	1/2
	1/2	1/2

0	1/2	0
1	1/2	0
	1/2	1/2

Moreover, the RATTLE algorithm corresponds to a two-stage partitioned Runge–Kutta method with Lobatto IIIa and Lobatto IIIb coefficients [30]. As such, the RATTLE algorithm is symmetric, symplectic and convergent of order two, see Theorem 1.3 in [27]. Furthermore, an extension to bilaterally constrained mechanical systems on nonlinear configuration spaces with Lie group structure has been proposed recently in [31].

A nonsmooth RATTLE scheme for multibody systems with frictional unilateral constraints has been proposed in [32]. The scheme of [32] differs in two ways. Firstly, the non-impulsive forces not related to contact, e.g., spring forces, dashpot forces, gyroscopic accelerations, are only present in the first stage and not distributed over both stages as in the classical RATTLE scheme [33]. Moreover, the mass matrix is only evaluated at the beginning of the time step for both stages. Thereby, the scheme cannot be interpreted as partitioned Runge–Kutta method and possibly looses second-order convergence in smooth phases. Secondly, the contact percussions appearing in the impact law [32, eq. (21e)] do not coincide with the velocity update given by the sum of eq. (21b) and eq. (21d) in [32]. The latter may result in a violation of the intended impact law.

This paper presents an extension to the RATTLE algorithm for nonsmooth mechanical systems with frictional unilateral constraints (i.e. frictional contact). In Section 2, the governing equations describing mechanical systems with nonsmooth frictional unilateral constraints are introduced. The RATTLE algorithm for such systems is derived in Section 3. In the subsequent section, implementation details are discussed. Finally, the algorithm is validated using a selection of representative benchmark examples in Section 5. The conclusions can be found in the last section.

2. Mechanical systems with frictional unilateral constraints

Consider a finite-dimensional mechanical system whose state is described by the generalized positions $\boldsymbol{q}(t) \in \mathbb{R}^{n_q}$ and by the generalized velocities $\boldsymbol{u}(t) \in \mathbb{R}^{n_u}$, which are both functions of time $t \in \mathbb{R}$. The relation between positions and velocities is a consequence of the kinematics of the system and is in general of the form

$$\mathrm{d}\boldsymbol{q} = \dot{\boldsymbol{q}}(t,\boldsymbol{q},\boldsymbol{u})\,\mathrm{d}t\,, \quad \text{where} \quad \dot{\boldsymbol{q}}(t,\boldsymbol{q},\boldsymbol{u}) = \boldsymbol{B}(t,\boldsymbol{q})\boldsymbol{u} + \boldsymbol{\beta}(t,\boldsymbol{q}) \tag{1}$$

denotes the kinematic differential equation with $\boldsymbol{B}(t,\boldsymbol{q}) \in \mathbb{R}^{n_q \times n_u}$, $\boldsymbol{\beta}(t,\boldsymbol{q}) \in \mathbb{R}^{n_q}$ and $n_u \leq n_q$.

In addition to the applied forces, the mechanical system is subjected to bilateral and frictional unilateral constraints. Its dynamics is then described by the equality of measures [1–3,5]

$$\begin{aligned}\boldsymbol{M}(t,\boldsymbol{q})\,\mathrm{d}\boldsymbol{u} &= \boldsymbol{h}(t,\boldsymbol{q},\boldsymbol{u})\,\mathrm{d}t + \boldsymbol{W}_g(t,\boldsymbol{q})\mathrm{d}\boldsymbol{P}_g + \boldsymbol{W}_\gamma(t,\boldsymbol{q})\mathrm{d}\boldsymbol{P}_\gamma + \boldsymbol{W}_N(t,\boldsymbol{q})\mathrm{d}\boldsymbol{P}_N + \boldsymbol{W}_F(t,\boldsymbol{q})\mathrm{d}\boldsymbol{P}_F \\ &= \boldsymbol{h}(t,\boldsymbol{q},\boldsymbol{u})\,\mathrm{d}t + \boldsymbol{W}(t,\boldsymbol{q})\mathrm{d}\boldsymbol{P}\,,\end{aligned} \tag{2}$$

which links the change in velocity $\mathrm{d}\boldsymbol{u}$ to the forces acting on the system. Therein, $\boldsymbol{M}(t,\boldsymbol{q}) \in \mathbb{R}^{n_u \times n_u}$ denotes the symmetric mass matrix, possibly depending explicitly on time t and on the generalized positions $\boldsymbol{q}$. For $\square \in \{g,\gamma,N,F\}$, the generalized force directions $\boldsymbol{W}_\square \in \mathbb{R}^{n_u \times n_\square}$ and percussion measures $\mathrm{d}\boldsymbol{P}_\square \in \mathbb{R}^{n_\square}$ are gathered in $\boldsymbol{W} = (\boldsymbol{W}_g\ \boldsymbol{W}_\gamma\ \boldsymbol{W}_N\ \boldsymbol{W}_F) \in \mathbb{R}^{n_u \times n_P}$ and[1] $\mathrm{d}\boldsymbol{P} = (\mathrm{d}\boldsymbol{P}_g, \mathrm{d}\boldsymbol{P}_\gamma, \mathrm{d}\boldsymbol{P}_N, \mathrm{d}\boldsymbol{P}_F) \in \mathbb{R}^{n_P}$, respectively, where $n_P = n_g + n_\gamma + n_N + n_F$ denotes the total number of constraints. All forces which are neither constraint nor contact forces, such as spring forces, dashpot forces and gyroscopic terms, are assumed to be nonimpulsive and are contained in $\boldsymbol{h}(t,\boldsymbol{q},\boldsymbol{u}) \in \mathbb{R}^{n_u}$. Following [1], the percussion measures $\mathrm{d}\boldsymbol{P}_\square$ combine the effects of nonimpulsive forces $\lambda_\square$ and impulsive forces $\boldsymbol{\Lambda}_\square$ in the sense that

$$\mathrm{d}\boldsymbol{P}_\square = \lambda_\square\,\mathrm{d}t + \boldsymbol{\Lambda}_\square \mathrm{d}\mu\,, \tag{3}$$

where $\mathrm{d}\mu$ denotes the atomic measure that can be interpreted as the sum of Dirac point measures $\mathrm{d}\delta_{t_i}$,

$$\mathrm{d}\mu = \sum_i \mathrm{d}\delta_{t_i}\,, \quad \int_{[t_a,t_b]} \mathrm{d}\delta_{t_i} = \begin{cases} 1 & t_i \in [t_a,t_b]\,, \\ 0 & t_i \notin [t_a,t_b]\,. \end{cases} \tag{4}$$

The generalized percussion measures $\boldsymbol{W}_g\mathrm{d}\boldsymbol{P}_g$ and $\boldsymbol{W}_\gamma\mathrm{d}\boldsymbol{P}_\gamma$ in (2) contain the perfect constraint forces of the bilateral position and velocity level constraints

$$\boldsymbol{g}(t,\boldsymbol{q}) = 0 \quad \text{and} \quad \boldsymbol{\gamma}(t,\boldsymbol{q},\boldsymbol{u}) = \boldsymbol{W}_\gamma{}^{\mathrm{T}}(t,\boldsymbol{q})\,\boldsymbol{u} + \boldsymbol{\chi}_\gamma(t,\boldsymbol{q}) = 0\,, \tag{5}$$

respectively. Using the kinematic differential equation (1), the time derivative of the bilateral constraints on position level is written as

$$\begin{aligned}\dot{\boldsymbol{g}}(t,\boldsymbol{q},\boldsymbol{u}) &= \frac{\partial \boldsymbol{g}}{\partial \boldsymbol{q}}(t,\boldsymbol{q})\,\dot{\boldsymbol{q}} + \frac{\partial \boldsymbol{g}}{\partial t}(t,\boldsymbol{q}) \overset{(1)}{=} \frac{\partial \boldsymbol{g}}{\partial \boldsymbol{q}}(t,\boldsymbol{q})\Big(\boldsymbol{B}(t,\boldsymbol{q})\boldsymbol{u} + \boldsymbol{\beta}(t,\boldsymbol{q})\Big) + \frac{\partial \boldsymbol{g}}{\partial t}(t,\boldsymbol{q}) \\ &= \boldsymbol{W}_g{}^{\mathrm{T}}(t,\boldsymbol{q})\,\boldsymbol{u} + \boldsymbol{\chi}_g(t,\boldsymbol{q})\,.\end{aligned} \tag{6}$$

Hence, the generalized force directions for bilateral constraints on position and velocity level are given by

$$\boldsymbol{W}_g{}^{\mathrm{T}} = \frac{\partial \dot{\boldsymbol{g}}}{\partial \boldsymbol{u}} = \frac{\partial \boldsymbol{g}}{\partial \boldsymbol{q}}\boldsymbol{B} \quad \text{and} \quad \boldsymbol{W}_\gamma{}^{\mathrm{T}} = \frac{\partial \boldsymbol{\gamma}}{\partial \boldsymbol{u}}\,. \tag{7}$$

The not yet discussed generalized percussion measures of (2), i.e., $\boldsymbol{W}_N\mathrm{d}\boldsymbol{P}_N + \boldsymbol{W}_F\mathrm{d}\boldsymbol{P}_F$, contain the force measures describing the frictional unilateral constraints. Their corresponding force laws can be described by normal cone inclusions [2,3,34,35]. Consider a pair of contact points on either contacting body, which we will simply refer to as contact k. Let $g_N^k(t,\boldsymbol{q})$ be the real-valued gap function describing the signed distance between the tangent planes of the pairs of contact points. The impenetrability of contact k is enforced by the perfect unilateral constraint $g_N^k \geq 0$. The contact is open if $g_N^k > 0$, i.e., the contacting bodies are separated. Excluding distance effects (e.g. magnetic or gravitational forces), the contact force $\lambda_N^k = 0$ is zero for an open contact. We speak of a closed contact if $g_N^k = 0$, i.e, the bodies are touching. The bodies are penetrating each other if $g_N^k < 0$. For non-adhesive contacting bodies this implies a non-negative contact force $\lambda_N^k \geq 0$. A graphical illustration of this contact law, known as Signorini's law, is depicted in Fig. 1(a). It can be equivalently stated as normal cone inclusion to the set $\mathbb{R}_0^- = \{x \in \mathbb{R} \,|\, x \leq 0\}$ of non-positive real numbers or as inequality complementarity condition

$$g_N^k(t,\boldsymbol{q}) \in \mathcal{N}_{\mathbb{R}_0^-}(-\lambda_N^k) \quad \Longleftrightarrow \quad g_N^k(t,\boldsymbol{q}) \geq 0\,, \quad \lambda_N^k \geq 0\,, \quad g_N^k(t,\boldsymbol{q})\,\lambda_N^k = 0\,, \tag{8}$$

where $\mathcal{N}_C(\boldsymbol{x}) = \{\boldsymbol{y} \in \mathbb{R}^f \,\big|\, \boldsymbol{y}^{\mathrm{T}}(\boldsymbol{x}^* - \boldsymbol{x}) \leq 0,\ \forall \boldsymbol{x}^* \in C\}$ denotes the normal cone to the closed, convex and non-empty set $C \subset \mathbb{R}^f$ evaluated at $\boldsymbol{x} \in C$. Consequently, we can define the set of active (closed or penetrated) contacts as

$$A(t,\boldsymbol{q}) = \Big\{k = 1,\dots,n_N \,\Big|\, g_N^k(t,\boldsymbol{q}) \leq 0\Big\}\,, \tag{9}$$

together with its complement $A^c = \{1,\dots,n_N\} \setminus A$, which is called the set of inactive (open) contacts. For the later implementation of a numerical method, it is crucial to consider in (9) not only closed contacts but also the potential occurrence of penetrated contacts arising from drift problems or solutions that have not yet reached convergence. By gathering the gap functions of all contacts into a vector $\boldsymbol{g}_N(t,\boldsymbol{q}) \in \mathbb{R}^{n_N}$ similar to (6) using (1), the gap velocity is defined as

$$\begin{aligned}\dot{\boldsymbol{g}}_N(t,\boldsymbol{q},\boldsymbol{u}) &= \frac{\partial \boldsymbol{g}_N}{\partial \boldsymbol{q}}(t,\boldsymbol{q})\,\dot{\boldsymbol{q}} + \frac{\partial \boldsymbol{g}_N}{\partial t}(t,\boldsymbol{q}) \overset{(1)}{=} \frac{\partial \boldsymbol{g}_N}{\partial \boldsymbol{q}}(t,\boldsymbol{q})\Big(\boldsymbol{B}(t,\boldsymbol{q})\boldsymbol{u} + \boldsymbol{\beta}(t,\boldsymbol{q})\Big) + \frac{\partial \boldsymbol{g}_N}{\partial t}(t,\boldsymbol{q}) \\ &= \boldsymbol{W}_N{}^{\mathrm{T}}(t,\boldsymbol{q})\,\boldsymbol{u} + \boldsymbol{\chi}_N(t,\boldsymbol{q})\,,\end{aligned} \tag{10}$$

where we have introduced the generalized force directions

$$\boldsymbol{W}_N{}^{\mathrm{T}} = \frac{\partial \dot{\boldsymbol{g}}_N}{\partial \boldsymbol{u}} = \frac{\partial \boldsymbol{g}_N}{\partial \boldsymbol{q}}\boldsymbol{B} \tag{11}$$

[1] We use the following notation: For $\boldsymbol{x} \in \mathbb{R}^{n\times 1} \cong \mathbb{R}^n$ and $\boldsymbol{y} \in \mathbb{R}^{m\times 1} \cong \mathbb{R}^m$, $(\boldsymbol{x},\boldsymbol{y}) := (\boldsymbol{x}^{\mathrm{T}}\ \boldsymbol{y}^{\mathrm{T}})^{\mathrm{T}} \in \mathbb{R}^{n+m\times 1} \cong \mathbb{R}^{n+m}$.

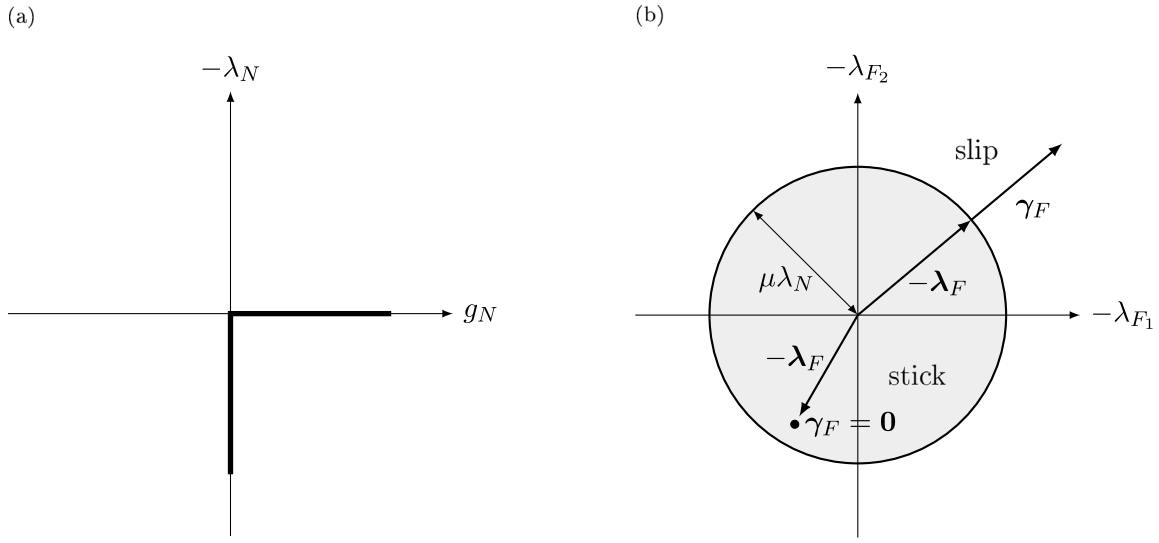

Fig. 1. Two different force laws of normal cone type. (a) Signorini's law $g_N \in \mathcal{N}_{\mathbb{R}_0^-}(-\lambda_N)$ and (b) spatial isotropic Coulomb friction $\boldsymbol{\gamma}_F \in \mathcal{N}_{B_2(\mu\lambda_N)}(-\boldsymbol{\lambda}_F)$. For $\|\boldsymbol{\lambda}_F\| \leq \mu\lambda_N$ this models *stick* and enforces the constraint $\boldsymbol{\gamma}_F = \mathbf{0}$. The case $\|\boldsymbol{\gamma}_F\| > 0$, denoted as *slip*, results in the force law $\boldsymbol{\lambda}_F = -\mu\lambda_N \boldsymbol{\gamma}_F / \|\boldsymbol{\gamma}_F\|$.

arising in (2). Following Section 10.4 of [4], Signorini's law (8) can also be formulated on velocity level as

$$\begin{cases} \dot{g}_N^k(t,\boldsymbol{q},\boldsymbol{u}) \in \mathcal{N}_{\mathbb{R}_0^-}(-\lambda_N^k) & \text{if } k \in A\,, \\ \lambda_N^k = 0 & \text{if } k \notin A\,. \end{cases} \tag{12}$$

The viability lemma of Moreau, Proposition 2.4 in [1], assets that (12) together with $g_N^k(t_0, \boldsymbol{q}(t_0)) \geq 0$ implies the unilateral constraint on position level

$$g_N^k(t,\boldsymbol{q}(t)) \geq 0\,, \quad \forall t \geq t_0\,, \tag{13}$$

which guaranties that the two contacting bodies do not penetrate each other for all future time.

Let $\boldsymbol{u}^-(t) = \lim_{\tau \uparrow t} \boldsymbol{u}(\tau)$ and $\boldsymbol{u}^+(t) = \lim_{\tau \downarrow t} \boldsymbol{u}(\tau)$ denote the left and right limits of the velocity, respectively. For active contacts, i.e., $k \in A(t,\boldsymbol{q})$, a generalized Newton-type impact law is equivalently stated as normal cone inclusion to the set $\mathbb{R}_0^-$ or as inequality complementarity condition

$$\xi_N^k(t,\boldsymbol{q},\boldsymbol{u}^-,\boldsymbol{u}^+) \in \mathcal{N}_{\mathbb{R}_0^-}(-\Lambda_N^k) \quad \Longleftrightarrow \quad \xi_N^k(t,\boldsymbol{q},\boldsymbol{u}^-,\boldsymbol{u}^+) \geq 0\,, \quad \Lambda_N^k \geq 0\,, \quad \xi_N^k(t,\boldsymbol{q},\boldsymbol{u}^-,\boldsymbol{u}^+)\,\Lambda_N^k = 0\,. \tag{14}$$

For a given restitution coefficient $0 \leq e_N^k \leq 1$ of the kth normal contact and for a strictly positive impulsive force $\Lambda_N^k > 0$, this imposes the classical Newtonian impact law

$$\xi_N^k(t,\boldsymbol{q},\boldsymbol{u}^-,\boldsymbol{u}^+) = \dot{g}_N^k(t,\boldsymbol{q},\boldsymbol{u}^+) + e_N^k\, \dot{g}_N^k(t,\boldsymbol{q},\boldsymbol{u}^-) = 0 \tag{15}$$

and encompasses superfluous contact for which $\Lambda_N^k = 0$ and $\xi_N^k \geq 0$, as detailed in Ref. [35].

Let the tangential velocity $\boldsymbol{\gamma}_F^k(t,\boldsymbol{q},\boldsymbol{u}) \in \mathbb{R}^2$ describe the relative velocity of the pair of contact points in the tangent plane. For a contact k, set-valued friction can be described by the normal cone inclusion

$$\boldsymbol{\gamma}_F^k(t,\boldsymbol{q},\boldsymbol{u}) \in \mathcal{N}_{C_F^k(\lambda_N^k)}(-\boldsymbol{\lambda}_F^k)\,, \tag{16}$$

where $C_F^k(\lambda_N^k)$ denotes the set of admissible (negative) friction forces. For isotropic Coulomb friction with friction coefficient $\mu^k > 0$, this set is given by

$$C_F^k(\lambda_N^k) = B_2(\mu^k \lambda_N^k) \quad \text{with} \quad B_f(r) = \{\boldsymbol{x} \in \mathbb{R}^f \mid \max(0,r) \geq \|\boldsymbol{x}\|\}\,. \tag{17}$$

A graphical visualization of spatial isotropic Coulomb friction is given in Fig. 1(b). The use of ball-like force reservoirs (17) with $f = 3$ and augmenting $\boldsymbol{\gamma}_F$ and $\boldsymbol{\lambda}_F$ in (16) by a relative angular velocity and a frictional torque, respectively, enables the formulation of an approximated Coulomb–Contensou friction, see [36]. This approach will be applied for the tippedisk example in Section 5. Similar to the normal direction (15), we introduce the kinematic quantity

$$\boldsymbol{\xi}_F^k(t,\boldsymbol{q},\boldsymbol{u}^-,\boldsymbol{u}^+) = \boldsymbol{\gamma}_F^k(t,\boldsymbol{q},\boldsymbol{u}^+) + e_F^k\, \boldsymbol{\gamma}_F^k(t,\boldsymbol{q},\boldsymbol{u}^-) \tag{18}$$

with a tangential restitution coefficient $0 \leq e_F^k \leq 1$. This allows to combine the friction law (16) with a Newton-type impact law in tangential direction by the normal cone inclusion

$$\boldsymbol{\xi}_F^k(t,\boldsymbol{q},\boldsymbol{u}^-,\boldsymbol{u}^+) \in \mathcal{N}_{C_F^k(\Lambda_N^k)}(-\boldsymbol{\Lambda}_F^k)\,. \tag{19}$$

For more details about the introduced contact model and impact laws we refer to [4,34,35,37].

3. Time discretization of the dynamics

Following Moreau [1], we will assume the generalized positions $\boldsymbol{q}(t)$ to be absolutely continuous, whereas the generalized velocities $\boldsymbol{u}(t)$ and percussions $\boldsymbol{P}(t)$ are assumed to be of special locally bounded variation. For a constant time step Δt, we introduce the notation $t_{n+\alpha} = t_n + \alpha\Delta t$ with $0 \leq \alpha \leq 1$ as well as the time interval $I_n = (t_n, t_{n+1}]$. Considering the velocity $\boldsymbol{u}(t) = \lim_{\tau \downarrow t} \boldsymbol{u}(\tau)$ as a right-continuous function, the dynamics of the system (2) determines the velocity at a time t_{n+1} as

$$\boldsymbol{u}(t_{n+1}) = \boldsymbol{u}(t_n) + \int_{I_n} \mathrm{d}\boldsymbol{u} \overset{(2)}{=} \boldsymbol{u}(t_n) + \int_{I_n} \boldsymbol{M}^{-1} \left(\boldsymbol{h}\, \mathrm{d}t + \boldsymbol{W}\, \mathrm{d}\boldsymbol{P} \right). \tag{20}$$

Also, the percussion $\boldsymbol{P}(t) = \lim_{\tau \downarrow t} \boldsymbol{P}(\tau)$ is considered as a right-continuous function. Its value at a time t_{n+1} can be written as the integrated percussion measure $\mathrm{d}\boldsymbol{P}$ in accordance with

$$\boldsymbol{P}(t_{n+1}) = \boldsymbol{P}(t_n) + \int_{I_n} \mathrm{d}\boldsymbol{P}\,. \tag{21}$$

Using the kinematic differential equation (1), the position $\boldsymbol{q}$ of the system at t_{n+1} is

$$\boldsymbol{q}(t_{n+1}) = \boldsymbol{q}(t_n) + \int_{I_n} \mathrm{d}\boldsymbol{q} = \boldsymbol{q}(t_n) + \int_{I_n} \dot{\boldsymbol{q}}(t, \boldsymbol{q}, \boldsymbol{u})\, \mathrm{d}t\,. \tag{22}$$

Let $\boldsymbol{q}_n$, $\boldsymbol{u}_n$ and $\boldsymbol{P}_n$ denote the approximants for the position, velocity and percussion at some time instant t_n, respectively. The integration of (20) is split into two half-steps in agreement with $I_n = I_n^{1\mathrm{st}} \cup I_n^{2\mathrm{nd}} = (t_n, t_{n+1/2}] \cup (t_{n+1/2}, t_{n+1}]$. Introducing an implicit midpoint velocity $\boldsymbol{u}_{n+1/2}$, we propose the approximation

$$\int_{I_n^{1\mathrm{st}}} \boldsymbol{M}^{-1} \left(\boldsymbol{h}\, \mathrm{d}t + \boldsymbol{W}\, \mathrm{d}\boldsymbol{P} \right) \approx \boldsymbol{M}_n^{-1} \left(\frac{\Delta t}{2} \boldsymbol{h}(t_n, \boldsymbol{q}_n, \boldsymbol{u}_{n+1/2}) + \boldsymbol{W}_n \left(\boldsymbol{P}_{n+1/2} - \boldsymbol{P}_n \right) \right) \tag{23a}$$

$$\int_{I_n^{2\mathrm{nd}}} \boldsymbol{M}^{-1} \left(\boldsymbol{h}\, \mathrm{d}t + \boldsymbol{W}\, \mathrm{d}\boldsymbol{P} \right) \approx \boldsymbol{M}_{n+1}^{-1} \left(\frac{\Delta t}{2} \boldsymbol{h}(t_{n+1}, \boldsymbol{q}_{n+1}, \boldsymbol{u}_{n+1/2}) + \boldsymbol{W}_{n+1} \left(\boldsymbol{P}_{n+1} - \boldsymbol{P}_{n+1/2} \right) \right), \tag{23b}$$

for the integration of (20). For the sake of compactness we write $\boldsymbol{M}_n = \boldsymbol{M}(t_n, \boldsymbol{q}_n)$, a notational abbreviation that is analogously applied for the other functions. To further lighten the notation in (23a) and (23b), we use

$$\Delta \boldsymbol{P}_{n+1}^{1\mathrm{st}} = \boldsymbol{P}_{n+1/2} - \boldsymbol{P}_n\,, \quad \Delta \boldsymbol{P}_{n+1}^{2\mathrm{nd}} = \boldsymbol{P}_{n+1} - \boldsymbol{P}_{n+1/2} \quad \text{and} \quad \Delta \boldsymbol{P}_{n+1} = \boldsymbol{P}_{n+1} - \boldsymbol{P}_n \tag{24}$$

for the percussion increments of each half-step and the respective increments over the whole interval I_n. Substituting (23a) and (23b) into (20) results in the two velocity updates

$$\boldsymbol{u}_{n+1/2} = \boldsymbol{u}_n + \boldsymbol{M}_n^{-1} \left(\frac{\Delta t}{2} \boldsymbol{h}(t_n, \boldsymbol{q}_n, \boldsymbol{u}_{n+1/2}) + \boldsymbol{W}_n \Delta \boldsymbol{P}_{n+1}^{1\mathrm{st}} \right) \tag{25a}$$

$$\boldsymbol{u}_{n+1} = \boldsymbol{u}_{n+1/2} + \boldsymbol{M}_{n+1}^{-1} \left(\frac{\Delta t}{2} \boldsymbol{h}(t_{n+1}, \boldsymbol{q}_{n+1}, \boldsymbol{u}_{n+1/2}) + \boldsymbol{W}_{n+1} \Delta \boldsymbol{P}_{n+1}^{2\mathrm{nd}} \right). \tag{25b}$$

Inserting (25a) into (25b)

$$\begin{aligned} \boldsymbol{u}_{n+1} = \boldsymbol{u}_n &+ \boldsymbol{M}_n^{-1} \left(\frac{\Delta t}{2} \boldsymbol{h}(t_n, \boldsymbol{q}_n, \boldsymbol{u}_{n+1/2}) + \boldsymbol{W}_n \Delta \boldsymbol{P}_{n+1}^{1\mathrm{st}} \right) \\ &+ \boldsymbol{M}_{n+1}^{-1} \left(\frac{\Delta t}{2} \boldsymbol{h}(t_{n+1}, \boldsymbol{q}_{n+1}, \boldsymbol{u}_{n+1/2}) + \boldsymbol{W}_{n+1} \Delta \boldsymbol{P}_{n+1}^{2\mathrm{nd}} \right) \end{aligned} \tag{26}$$

reveals that the velocity update $\boldsymbol{u}_n \mapsto \boldsymbol{u}_{n+1}$ is given by a combination of trapezoidal rule of the positions $\boldsymbol{q}_n$, $\boldsymbol{q}_{n+1}$ and an implicit midpoint rule involving the midpoint velocity $\boldsymbol{u}_{n+1/2}$ for the approximation of (20).

For the position update, the integral in (22) is also approximated using a combination of trapezoidal rule of positions $\boldsymbol{q}_n$, $\boldsymbol{q}_{n+1}$ and an implicit midpoint rule of the velocity $\boldsymbol{u}_{n+1/2}$. Specifically,

$$\boldsymbol{q}_{n+1} = \boldsymbol{q}_n + \frac{\Delta t}{2} \left(\dot{\boldsymbol{q}}(t_n, \boldsymbol{q}_n, \boldsymbol{u}_{n+1/2}) + \dot{\boldsymbol{q}}(t_{n+1}, \boldsymbol{q}_{n+1}, \boldsymbol{u}_{n+1/2}) \right). \tag{27}$$

With this approximation, it is evident from (25) that $\boldsymbol{q}_{n+1}$ is only influenced by the midpoint velocity $\boldsymbol{u}_{n+1/2}$ and hence by the increments in percussions $\Delta \boldsymbol{P}_{n+1}^{1\mathrm{st}} = \boldsymbol{P}_{n+1/2} - \boldsymbol{P}_n$ of the first half-step. The increments $\Delta \boldsymbol{P}_{n+1}^{2\mathrm{nd}} = \boldsymbol{P}_{n+1} - \boldsymbol{P}_{n+1/2}$ of the second half-step only affects the velocity update for $\boldsymbol{u}_{n+1}$. This "splitting", which is typical for RATTLE, allows to independently satisfy constraint conditions on two different kinematic levels. Specifically, the classical RATTLE algorithm enforces perfect bilateral constraints on position level and their underlying (or hidden) constraints on velocity level. The nonsmooth RATTLE algorithm, proposed here and essentially given by (26) and (27), is to be complemented by force laws for the percussion increments (24) which serve as Lagrange multipliers. We subsequently introduce how the discrete force laws from Section 2 are formulated on both kinematic levels.

As just mentioned, the Lagrange multipliers $\Delta \boldsymbol{P}_{g,n+1}^{1\mathrm{st}}, \Delta \boldsymbol{P}_{g,n+1}^{2\mathrm{nd}} \in \mathbb{R}^{n_g}$ enforce the perfect bilateral constraints on position and velocity level at the end of the time step, i.e.,

$$\boldsymbol{g}(t_{n+1}, \boldsymbol{q}_{n+1}) = 0\,, \tag{28a}$$

$$\dot{\boldsymbol{g}}(t_{n+1}, \boldsymbol{q}_{n+1}, \boldsymbol{u}_{n+1}) = 0\,, \tag{28b}$$

see Section 7.1.4 of Ref. [27]. Similarly, with $\Delta \boldsymbol{P}^{1\text{st}}_{\gamma,n+1}, \Delta \boldsymbol{P}^{2\text{nd}}_{\gamma,n+1} \in \mathbb{R}^{n_\gamma}$ we impose the bilateral constraints on velocity level for the midpoint velocity $\boldsymbol{u}_{n+1/2}$ and the final velocity $\boldsymbol{u}_{n+1}$, i.e.,

$$\boldsymbol{\gamma}(t_{n+1}, \boldsymbol{q}_{n+1}, \boldsymbol{u}_{n+1/2}) = 0\,, \tag{29a}$$

$$\boldsymbol{\gamma}(t_{n+1}, \boldsymbol{q}_{n+1}, \boldsymbol{u}_{n+1}) = 0\,. \tag{29b}$$

In what follows, we assume that if the contact k is active at the end of the time step, i.e., $k \in A_{n+1} = A(t_{n+1}, \boldsymbol{q}_{n+1})$, then it has been active during the whole time step $I_n = (t_n, t_{n+1}]$. Furthermore, we assume ξ^k_N to be constant on I_n and to correspond to

$$\xi^k_{N,n+1} = \dot{g}^k_N(t_{n+1}, \boldsymbol{q}_{n+1}, \boldsymbol{u}_{n+1}) + e^k_N\, \dot{g}^k_N(t_n, \boldsymbol{q}_n, \boldsymbol{u}_n)\,, \tag{30}$$

which is regarded as a discrete approximation of (15) over one time step. The velocity of the system is continuous between velocity jumps, implying $\dot{g}^{k+}_N = \dot{g}^{k-}_N = \dot{g}^k_N$ for almost all t. Hence, in such cases it holds that

$$(1 + e^k_N)\dot{g}^k_N = \dot{g}^{k+}_N + e^k_N \dot{g}^{k-}_N = \xi^k_N \tag{31}$$

and we can write Signorini's law on velocity level (12) using ξ^k_N instead of $\dot{g}^k_N$. Using all these preliminary assumptions together with Proposition 2 of [18] we are allowed to combine Signorini's law on velocity level (12) and the Newton-type impact law in normal direction (14) as

$$\begin{cases} \xi^k_{N,n+1} \in \mathcal{N}_{\mathbb{R}^-_0}(-\int_{I_n} \mathrm{d}P^k_N) = \mathcal{N}_{\mathbb{R}^-_0}(\Delta P^k_{N,n+1}) & \text{if } k \in A\,, \\ 0 = \int_{I_n} \mathrm{d}P^k_N = \Delta P^k_{N,n+1} & \text{if } k \notin A\,. \end{cases} \tag{32}$$

A discussion of how this is done in detail as well as an interpretation of the integrated contact law can be found in Section 6 of Ref. [18]. Since the position $\boldsymbol{q}_{n+1}$ is only affected by the mid-point velocity $\boldsymbol{u}_{n+1/2}$ of the first half-step (25a), we use $\Delta \boldsymbol{P}^{1\text{st}}_{N,n+1} = \boldsymbol{P}_{N,n+1/2} - \boldsymbol{P}_{N,n}$ to satisfy an integrated formulation of Signorini's law on position level over the first half-step, i.e.,

$$g^k_N(t_{n+1}, \boldsymbol{q}_{n+1}) \in \mathcal{N}_{\mathbb{R}^-_0}(-\textstyle\int_{I^{1\text{st}}_n} \mathrm{d}P^k_N) = \mathcal{N}_{\mathbb{R}^-_0}(\Delta P^{1\text{st},k}_{N,n+1})\,. \tag{33}$$

To summarize, the normal direction of the temporally discretized contact and impact laws (8) and (14) are given by (32) and (33). Hence, the numerical method imposes Signorini's law on position level and the Newton-type impact law in an integral sense over the whole time step I_n, where $\boldsymbol{u}_n$ and $\boldsymbol{u}_{n+1}$ are regarded as the pre- and post-impact velocities, respectively.

For the discretization of the set-valued friction law a similar path is taken. Using the same assumptions as above, we can combine the friction law (16) and the Newton-type impact law in tangential direction (19) as

$$\boldsymbol{\xi}^k_{F,n+1} \in \mathcal{N}_{C^k_F(\int_{I_n} \mathrm{d}P^k_N)}(-\textstyle\int_{I_n} \mathrm{d}\boldsymbol{P}^k_F) = \mathcal{N}_{C^k_F(\Delta P^k_{N,n+1})}\big(-\Delta \boldsymbol{P}^k_{F,n+1}\big)\,, \tag{34}$$

where we have approximated (18) as

$$\boldsymbol{\xi}^k_{F,n+1} = \boldsymbol{\gamma}_F(t_{n+1}, \boldsymbol{q}_{n+1}, \boldsymbol{u}_{n+1}) + e^k_F\, \boldsymbol{\gamma}^k_F(t_n, \boldsymbol{q}_n, \boldsymbol{u}_n)\,. \tag{35}$$

Moreover, the mid-point velocity $\boldsymbol{u}_{n+1/2}$ is forced to satisfy the integrated friction law over the first half-step

$$\boldsymbol{\gamma}^k_F(t_{n+1}, \boldsymbol{q}_{n+1}, \boldsymbol{u}_{n+1/2}) \in \mathcal{N}_{C^k_F(\int_{I^{1\text{st}}_n} \mathrm{d}P^k_N)}(-\textstyle\int_{I^{1\text{st}}_n} \mathrm{d}\boldsymbol{P}^k_F) = \mathcal{N}_{C^k_F(\Delta P^{1\text{st},k}_{N,n+1})}\big(-\Delta \boldsymbol{P}^{1\text{st},k}_{F,n+1}\big)\,. \tag{36}$$

Consequently, the discrete friction laws are given by (34) and (36). They satisfy a set-valued friction law at the mid-point velocity $\boldsymbol{u}_{n+1/2}$ and a combination of set-valued friction law and a Newton-type impact law in an integral sense, where $\boldsymbol{u}_n$ and $\boldsymbol{u}_{n+1}$ are regarded as the pre- and post-impact velocities, respectively.

4. Implementation of the numerical algorithm

The computation of one time step $(t_n, \boldsymbol{q}_n, \boldsymbol{u}_n, \boldsymbol{P}_n) \mapsto (t_{n+1}, \boldsymbol{q}_{n+1}, \boldsymbol{u}_{n+1}, \boldsymbol{P}_{n+1})$ of the proposed nonsmooth RATTLE algorithm can be split into two decoupled stages. Both stages can be brought into residual form and are then solved using a semismooth Newton method [18,38,39].

In order to reformulate the normal cone inclusions appearing in the discrete contact laws (32), (33), (34) and (36), we use the following equivalent relations. For two vectors $\boldsymbol{x}, \boldsymbol{y} \in \mathbb{R}^f$ and a closed, convex and non-empty set $C \subset \mathbb{R}^f$, it holds that

$$\boldsymbol{y} \in \mathcal{N}_C(-\boldsymbol{x}) \quad \Longleftrightarrow \quad \boldsymbol{0} = \boldsymbol{x} + \mathrm{prox}_C(r\boldsymbol{y} - \boldsymbol{x}) \quad \forall r > 0\,, \tag{37}$$

where

$$\mathrm{prox}_C : \mathbb{R}^f \to \mathbb{R}^f,\ \boldsymbol{a} \mapsto \mathrm{prox}_C(\boldsymbol{a}) = \underset{\boldsymbol{a}^* \in C}{\mathrm{argmin}}\big(\tfrac{1}{2}\|\boldsymbol{a} - \boldsymbol{a}^*\|^2\big) \tag{38}$$

is the proximal point function to C, see [5,18]. For the sets $C = \mathbb{R}^-_0$ and $C = B_f(r)$, the proximal point functions are given by

$$\mathrm{prox}_{\mathbb{R}^-_0}(x) = \min\{x, 0\} \quad \text{and} \quad \mathrm{prox}_{B_f(r)}(\boldsymbol{x}) = \begin{cases} \boldsymbol{x} & \text{if} \quad \boldsymbol{x} \in B_f(r)\,, \\ r\frac{\boldsymbol{x}}{\|\boldsymbol{x}\|} & \text{if} \quad \boldsymbol{x} \notin B_f(r)\,. \end{cases} \tag{39}$$

Hence, we can replace the normal cone inclusions (32), (33), (34) and (36) by the implicit functions (39).

For the first stage $(t_n, \boldsymbol{q}_n, \boldsymbol{u}_n, \boldsymbol{P}_n) \mapsto (t_{n+1}, \boldsymbol{q}_{n+1}, \boldsymbol{u}_{n+1/2}, \boldsymbol{P}_{n+1/2})$ the residual form $\boldsymbol{\Phi}_1(\boldsymbol{x}_1) = \boldsymbol{0}$ is given in terms of the vector of unknowns

$$\boldsymbol{x}_1 = (\boldsymbol{q}_{n+1}, \boldsymbol{u}_{n+1/2}, \Delta\boldsymbol{P}^{1\mathrm{st}}_{g,n+1}, \Delta\boldsymbol{P}^{1\mathrm{st}}_{\gamma,n+1}, \Delta\boldsymbol{P}^{1\mathrm{st}}_{N,n+1}, \Delta\boldsymbol{P}^{1\mathrm{st}}_{F,n+1}). \tag{40}$$

The residual gathers (25a), (27), (28a), (29a) and the implicit functions corresponding to (33) and (36) as

$$\boldsymbol{\Phi}_1(\boldsymbol{x}_1) = \begin{bmatrix} \boldsymbol{q}_{n+1} - \boldsymbol{q}_n - \frac{\Delta t}{2}\left(\dot{\boldsymbol{q}}(t_n, \boldsymbol{q}_n, \boldsymbol{u}_{n+1/2}) + \dot{\boldsymbol{q}}(t_{n+1}, \boldsymbol{q}_{n+1}, \boldsymbol{u}_{n+1/2})\right) \\ \boldsymbol{M}_n(\boldsymbol{u}_{n+1/2} - \boldsymbol{u}_n) - \left(\frac{\Delta t}{2}\boldsymbol{h}(t_n, \boldsymbol{q}_n, \boldsymbol{u}_{n+1/2}) + \boldsymbol{W}_n \Delta\boldsymbol{P}^{1\mathrm{st}}_{n+1}\right) \\ \boldsymbol{g}(t_{n+1}, \boldsymbol{q}_{n+1}) \\ \boldsymbol{\gamma}(t_{n+1}, \boldsymbol{q}_{n+1}, \boldsymbol{u}_{n+1/2}) \\ \Delta P^{1\mathrm{st},k}_{N,n+1} + \mathrm{prox}_{\mathbb{R}^-_0}\left(r^k g^k_N(t_{n+1}, \boldsymbol{q}_{n+1}) - \Delta P^{1\mathrm{st},k}_{N,n+1}\right) \\ \Delta\boldsymbol{P}^{1\mathrm{st},k}_{F,n+1} + \mathrm{prox}_{C^k_F(\Delta P^{1\mathrm{st},k}_{N,n+1})}\left(r^k \boldsymbol{\gamma}^k_F(t_{n+1}, \boldsymbol{q}_{n+1}, \boldsymbol{u}_{n+1/2}) - \Delta\boldsymbol{P}^{1\mathrm{st},k}_{F,n+1}\right) \end{bmatrix}, \tag{41}$$

where the last two lines indicate the unilateral constraint conditions for all contacts $k = 1, 2, \ldots, n_N$. In agreement with (24), we obtain $\boldsymbol{P}_{n+1/2} = \boldsymbol{P}_n + \Delta\boldsymbol{P}^{1\mathrm{st}}_{n+1}$. Introducing another vector of unknowns

$$\boldsymbol{x}_2 = (\boldsymbol{u}_{n+1}, \Delta\boldsymbol{P}^{2\mathrm{nd}}_{g,n+1}, \Delta\boldsymbol{P}^{2\mathrm{nd}}_{\gamma,n+1}, \Delta\boldsymbol{P}^{2\mathrm{nd}}_{N,n+1}, \Delta\boldsymbol{P}^{2\mathrm{nd}}_{F,n+1}), \tag{42}$$

the second stage $(t_{n+1}, \boldsymbol{q}_{n+1}, \boldsymbol{u}_{n+1/2}, \boldsymbol{P}_{n+1/2}) \mapsto (t_{n+1}, \boldsymbol{q}_{n+1}, \boldsymbol{u}_{n+1}, \boldsymbol{P}_{n+1})$ can be brought into residual form $\boldsymbol{\Phi}_2(\boldsymbol{x}_2) = \boldsymbol{0}$. It gathers (25b), (28b), (29b) and the implicit functions corresponding to (32) and (34) as

$$\boldsymbol{\Phi}_2(\boldsymbol{x}_2) = \begin{bmatrix} \boldsymbol{M}_{n+1}(\boldsymbol{u}_{n+1} - \boldsymbol{u}_{n+1/2}) - \left(\frac{\Delta t}{2}\boldsymbol{h}(t_{n+1}, \boldsymbol{q}_{n+1}, \boldsymbol{u}_{n+1/2}) + \boldsymbol{W}_{n+1}\Delta\boldsymbol{P}^{2\mathrm{nd}}_{n+1}\right) \\ \dot{\boldsymbol{g}}(t_{n+1}, \boldsymbol{q}_{n+1}, \boldsymbol{u}_{n+1}) \\ \boldsymbol{\gamma}(t_{n+1}, \boldsymbol{q}_{n+1}, \boldsymbol{u}_{n+1}) \\ \begin{cases} \Delta P^k_{N,n+1} + \mathrm{prox}_{\mathbb{R}^-_0}\left(r^k \xi^k_{N,n+1} - \Delta P^k_{N,n+1}\right) & \text{if } k \in A_{n+1} \\ \Delta P^k_{N,n+1} & \text{if } k \notin A_{n+1} \end{cases} \\ \Delta\boldsymbol{P}^k_{F,n+1} + \mathrm{prox}_{C^k_F(\Delta P^k_{N,n+1})}\left(r^k \boldsymbol{\xi}^k_{F,n+1} - \Delta\boldsymbol{P}^k_{F,n+1}\right) \end{bmatrix}, \tag{43}$$

where again the last two lines indicate the unilateral constraint conditions for all contacts $k = 1, 2, \ldots, n_N$. In agreement with (24), $\boldsymbol{P}_{n+1} = \boldsymbol{P}_n + \Delta\boldsymbol{P}_{n+1}$ with $\Delta\boldsymbol{P}_{n+1} = \Delta\boldsymbol{P}^{1\mathrm{st}}_{n+1} + \Delta\boldsymbol{P}^{2\mathrm{nd}}_{n+1}$. Since $\boldsymbol{q}_{n+1}$ is already determined in the first stage, the set of active contacts $A_{n+1} = A(t_{n+1}, \boldsymbol{q}_{n+1})$ does not change during the second stage. For inelastic contacts with $e_N = e_F = 0$, we can replace $\xi_{N,n+1}$ and $\boldsymbol{\xi}_{F,n+1}$ in (43) by $\gamma_N(t_{n+1}, \boldsymbol{q}_{n+1}, \boldsymbol{u}_{n+1})$ and $\boldsymbol{\gamma}_F(t_{n+1}, \boldsymbol{q}_{n+1}, \boldsymbol{u}_{n+1})$, respectively.

Eqs. (41) and (43) can be solved using a semismooth (nonsmooth) Newton method [18,38,39], where any regular element of the generalized Jacobian can be used. In order to control the chosen element of the generalized Jacobian and remove the dependency of the residual (generalized Jacobian) on the chosen proximal point parameters, an active-set formulation is beneficial [17–19]. Hence, the proximal point parameters are only present in the activation conditions of the residual and do not affect the accuracy of the computed residual (generalized Jacobian). An in-depth discussion *on solving contact problems with Coulomb friction* is given in [39]. Details of the active-set strategy and its relation to semi-smooth Newton methods are elaborated in [40].

In order to deal with scenarios where the generalized force directions become linearly dependent (redundant contacts), a popular strategy for solving (41) and (43) is given by fixed-point iterations [18,38,41,42]. Besides difficulties of choosing appropriate proximal point parameters that lead to a convergent fixed-point iteration, dealing with nonlinear equations as (41) results in a time consuming iterative method, since within each fixed-point iteration a nonlinear system of equations has to be solved.

5. Numerical validation

In this section, we present four different numerical examples to showcase the versatility and robustness of the proposed algorithm in handling various scenarios. The rotating bouncing ball example demonstrates the essentials of a numerical method applied on nonsmooth dynamical systems including impacts and friction. Subsequently, the ability of the proposed method to handle impulsive changes of bilateral constraint forces as well as a variety of high frequency contact patterns is investigated with a slider-crank mechanism. The third example demonstrates the convergence properties of the proposed method. For persistent frictional contact, second-order accuracy is obtained for the generalized positions and velocities. Finally, the tippedisk example shows that the method can handle nontrivial kinematic relations as well as a spatial friction law. For all examples, the maximum and average required Newton increments of both stages are reported in Table 1.

5.1. Rotating bouncing ball

Following [18,43], we investigate the motion of a homogeneous sphere of $R = 0.1$ and mass $m = 1$ subjected to gravitational forces with gravitational acceleration $g = 9.81$ falling on a horizontal plane, see Fig. 2. The sphere is constrained to move in the $\boldsymbol{e}^I_x$-$\boldsymbol{e}^I_y$-plane. Hence, it can be described by the generalized positions $\boldsymbol{q} = (x,\ y,\ \varphi)$. The vector ${}_I\boldsymbol{r}_{OS} = (x,\ y,\ 0)$ addresses the center of mass S with respect to the inertial basis I. Moreover, its orientation is described by the angle φ. The generalized velocities

Table 1
Maximum (max.) and average (avg.) required Newton iterations for all presented examples.

Example	Stage 1 (max.)	Stage 1 (avg.)	Stage 2 (max.)	Stage 2 (avg.)
Bouncing ball (case 1)	2	1.0066	1	0.9466
Bouncing ball (case 2)	3	1.0270	2	0.9466
Bouncing ball (case 3)	3	1.0270	2	0.6756
Slider-crank	5	2.2290	3	1.0081
Mass on slope (case 1)	2	1.2774	2	0.6463
Mass on slope (case 2)	2	1.1737	2	0.5945
Mass on slope (case 3)	4	1.3628	2	0.6859
Mass on slope (case 4)	5	1.2469	2	0.6737
Tippedisk	3	2.4103	2	2.0000

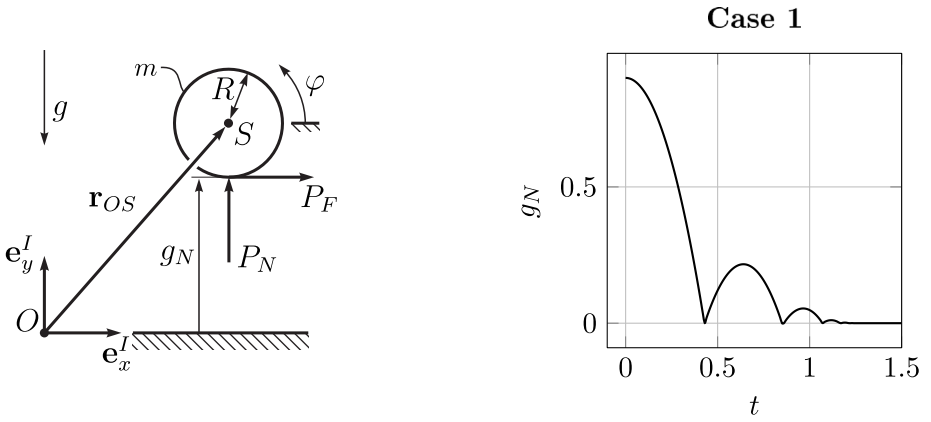

Fig. 2. Sketch of the bouncing ball system (left) and simulated time evolution of the contact distance for Case 1 (right).

$\boldsymbol{u} = (u_x,\ u_y,\ u_\varphi)$ are chosen to correspond to $\dot{\boldsymbol{q}}$ whenever the time derivative of the generalized positions exists. Consequently, the ingredients for the equality of measures (2) are given in terms of

$$\boldsymbol{M} = \operatorname{diag}(m,\ m,\ 2\ mR^2/5) \quad \text{and} \quad \boldsymbol{h} = (0,\ -mg,\ 0)\,. \tag{44}$$

For the description of planar Coulomb friction in line with (17), we chose $\mu = 0.2$ and $e_F = 0$. A number of different cases will be considered for the restitution coefficient in normal direction, e_N.

From this problem, three different scenarios were considered to validate the presented method. They share the same initial configuration given by $t_0 = 0$, $\boldsymbol{q}(t_0) = (0,\ 1,\ 0)$ and $\boldsymbol{u}(t_0) = (0,\ 0,\ \omega)$, such that the ball has an initial rotational velocity ω. The simulations were performed using a constant step-size $\Delta t = 10^{-2}$ together with the proximal point parameters $r_N = r_F = 0.1$. Using a semismooth Newton method, the nonlinear equations (41) and (43) where solved up to an absolute error of 10^{-8}.

Case 1:. Starting from rest ($\omega = 0$) and assuming elastic impacts with $e_N = 0.5$, the typical bouncing ball motion exhibiting the Zeno phenomenon is obtained. The simulation result shown in Fig. 2 confirms that the presented method can overcome accumulation points. Even for the moderate time step no penetration is obtained, since this is enforced by the method.

The subsequent two cases are used to test the behavior of the proposed algorithm with respect to friction forces. For both cases, we set $e_N = 0$ implying that once the contact closes it remains closed, i.e., the post impact velocity in normal direction vanishes, which allows us to validate friction. At the closing time instant a frictional impact occurs. Depending on the value of ω, two cases arise.

Case 2:. For a high initial rotational velocity ($\omega = 50$) sliding occurs after the impact. After undergoing a period of sliding contact, the ball slows down enough to enter into a slip-stick transition. At this point, the ball begins to move in a pure rolling motion. Since the rolling motion is characterized by constant velocities, no net forces are generated. Consequently, at the slip-stick transition, the non-impulsive friction force instantly drops to zero. Fig. 3 illustrates that the presented method perfectly replicates the described behavior.

Case 3:. In the third scenario, we selected a rotation velocity of $\omega = 10$, which was small enough to cause the ball to stick upon impact, exhibiting a pure rolling motion. Again, this behavior is described by zero tangential contact forces. As illustrated in Fig. 3, the numerical solution perfectly aligns with the results of [18].

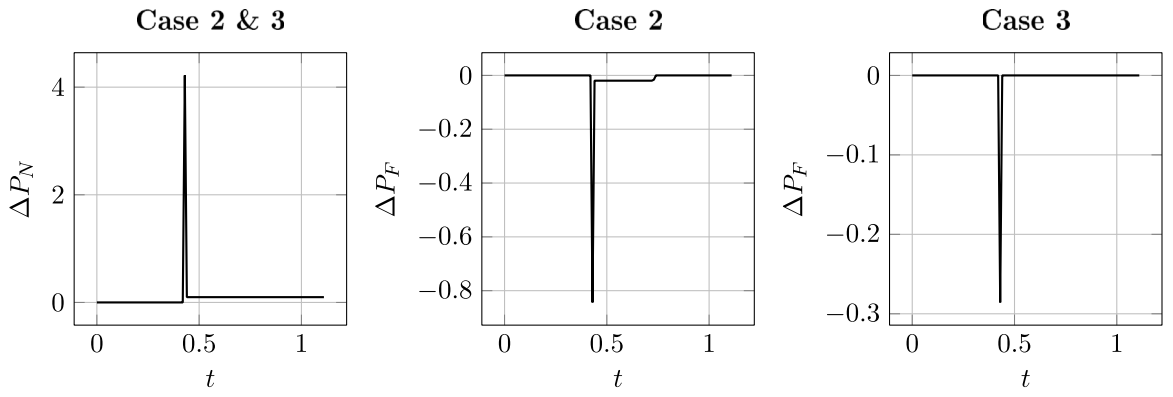

Fig. 3. Simulated normal and friction contact percussion increments for Case 2 ($\omega = 50$) and Case 3 ($\omega = 10$).

Table 2
Geometry and inertia properties of the slider-crank mechanism.

l_1	l_2	$a = 2b$	d	$m_1 = m_2$	m_3	θ_{S_1}	θ_{S_2}	θ_{S_3}	g
0.153	0.306	0.05	0.052	0.038	0.076	$7.4 \cdot 10^{-5}$	$5.9 \cdot 10^{-4}$	$2.7 \cdot 10^{-6}$	9.81

5.2. Slider-crank mechanism

Inspired by the investigations of [44], this example examines a slider-crank mechanism subjected to both unilateral and bilateral constraints, see Fig. 4. Hence, this example demonstrates the ability of the proposed method to handle impulsive changes of bilateral constraint forces as well as a variety of high frequency contact patterns. The mechanism is described by three independent rigid bodies with masses m_1, m_2, m_3 and inertia θ_{S_1}, θ_{S_2}, θ_{S_3} with respect to their centers of mass S_1, S_2, S_3. Each body is subjected to gravitational forces. In accordance with the notation from the previous example, we use the generalized positions $\boldsymbol{q} = (x_1,\ y_1,\ \varphi_1,\ x_2,\ y_2,\ \varphi_2,\ x_3,\ y_3,\ \varphi_3)$ and generalized velocities $\dot{\boldsymbol{q}} = \boldsymbol{u} = (u_{x_1},\ u_{y_1},\ u_{\varphi_1},\ u_{x_2},\ u_{y_2},\ u_{\varphi_2},\ u_{x_3},\ u_{y_3},\ u_{\varphi_3})$. The vectors ${}_I\boldsymbol{r}_{OS_i} = (x_i,\ y_i,\ 0)$, $i = 1, 2, 3$, address the center of masses S_i with respect to the inertial basis I and φ_i, $i = 1, 2, 3$, describe the bodies orientations with respect to the $\boldsymbol{e}_x^I$-axis. Consequently, the ingredients for the equality of measures (2) are given in terms of

$$\boldsymbol{M} = \operatorname{diag}(m_1,\ m_1,\ \theta_{S_1},\ m_2,\ m_2,\ \theta_{S_2},\ m_3,\ m_3,\ \theta_{S_3}) \tag{45}$$

and

$$\boldsymbol{h} = (0,\ -m_1\, g,\ 0,\ 0,\ -m_2\, g,\ 0,\ 0,\ -m_3\, g,\ 0)\,. \tag{46}$$

The rigid bodies are connected by the bilateral constraints

$$\boldsymbol{g}_1 = \begin{pmatrix} x_1 - \frac{l_1}{2}\cos\varphi_1 \\ y_1 - \frac{l_1}{2}\sin\varphi_1 \end{pmatrix},\ \boldsymbol{g}_2 = \begin{pmatrix} x_1 + \frac{l_1}{2}\cos\varphi_1 \\ y_1 + \frac{l_1}{2}\sin\varphi_1 \end{pmatrix} - \begin{pmatrix} x_2 - \frac{l_2}{2}\cos\varphi_2 \\ y_2 - \frac{l_2}{2}\sin\varphi_2 \end{pmatrix},\ \boldsymbol{g}_3 = \begin{pmatrix} x_2 + \frac{l_2}{2}\cos\varphi_2 \\ y_2 + \frac{l_2}{2}\sin\varphi_2 \end{pmatrix} - \begin{pmatrix} x_3 \\ y_3 \end{pmatrix}. \tag{47}$$

Each vertex of the slider is subjected to frictional contacts, described by the normal contact distances

$$\begin{aligned} g_{N_1} &= \frac{d}{2} - (y_3 - a\sin\varphi_3 + b\cos\varphi_3)\,, \quad g_{N_2} = \frac{d}{2} - (y_3 + a\sin\varphi_3 + b\cos\varphi_3) \\ g_{N_3} &= \frac{d}{2} + (y_3 - a\sin\varphi_3 - b\cos\varphi_3)\,, \quad g_{N_4} = \frac{d}{2} + (y_3 + a\sin\varphi_3 - b\cos\varphi_3) \end{aligned} \tag{48}$$

and the relative tangential contact velocities

$$\begin{aligned} \gamma_{F_1} &= u_{x_3} + u_{\varphi_3}(a\sin\varphi_3 - b\cos\varphi_3)\,, \quad \gamma_{F_2} = u_{x_3} - u_{\varphi_3}(a\sin\varphi_3 + b\cos\varphi_3) \\ \gamma_{F_3} &= u_{x_3} + u_{\varphi_3}(a\sin\varphi_3 + b\cos\varphi_3)\,, \quad \gamma_{F_4} = u_{x_3} - u_{\varphi_3}(a\sin\varphi_3 - b\cos\varphi_3) \end{aligned} \tag{49}$$

with $e_N = 0.4$, $e_F = 0$ and $\mu = 0.01$. Constraint derivatives and generalized force directions for both unilateral and bilateral constraints are obtained by differentiation of (47) to (49) with respect to time t and generalized velocities $\boldsymbol{u}$, respectively.

The geometry and inertia properties of the mechanism are listed in Table 2. The initial conditions were chosen as $t_0 = 0$, $\boldsymbol{q}_0 = \boldsymbol{q}(t_0) = (0.0765,\ 0,\ 0,\ 0.306,\ 0,\ 0,\ 0.459,\ 0,\ 0.017)$ and $\boldsymbol{u}_0 = \boldsymbol{u}(t_0) = (0,\ 11.475,\ 150,\ 0,\ 11.475,\ -75,\ 0,\ 0,\ 0)$. In order to get high-resolution results, the simulation was performed using a constant step-size $\Delta t = 10^{-4}$, although a ten times larger value could solve the problem without any convergence issues. We used the proximal point parameters $r_N = r_F = 0.1$ and solved the nonlinear equations (41) and (43) using a semismooth Newton method up to an absolute error of 10^{-8}.

Exemplary simulation results are depicted in Fig. 5. Since the simulation started with a small perturbation of the sliders orientation ($\varphi_3 \approx 1°$), it is apparent from Fig. 5(d), that the slider's orientation is stabilized after a small time lapse ($t \approx 0.01$).

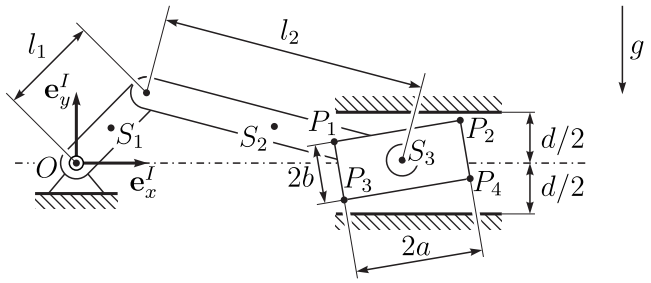

Fig. 4. Sketch of the slider-crank mechanism.

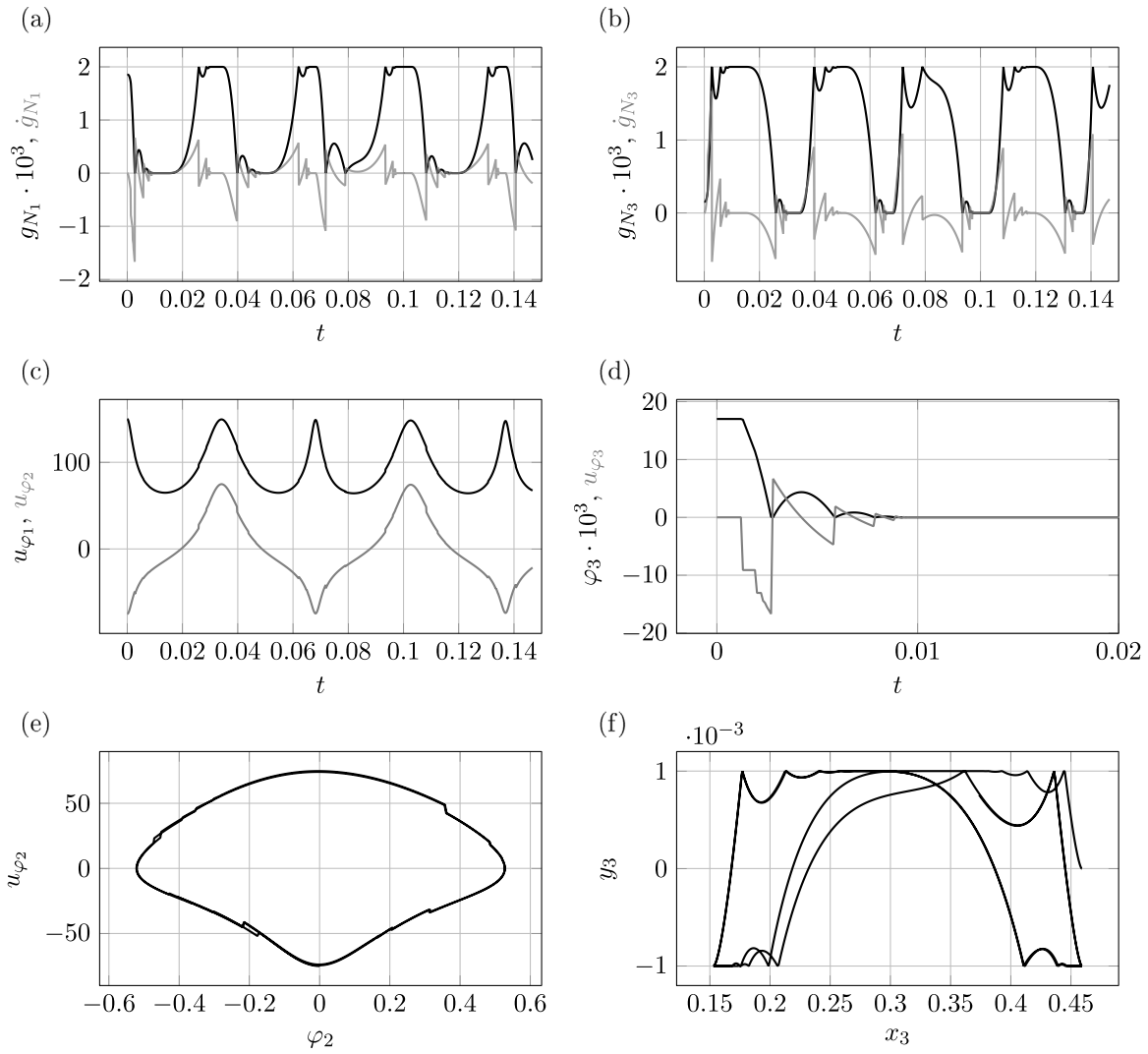

Fig. 5. Exemplary results of the slider-crank mechanism.

Afterwards, $\varphi_3 = u_{\varphi_3} \approx 0$ and the sliders center of mass moves according to Fig. 5(f) without any rotation. The time evolution of the velocities u_{φ_1} and u_{φ_2} is shown in Fig. 5(c). Neglecting dissipation, they show a periodic solution. An exemplary phase portrait of $(\varphi_2, u_{\varphi_2})$ is given in Fig. 5(e). Moreover, Fig. 5(a) and (b) show the evolution of two exemplary contact distances and their time derivatives. As enforced by the method, no penetration is present and whenever a contact is closed, the corresponding contact velocity satisfies a generalized impact Newton's law.

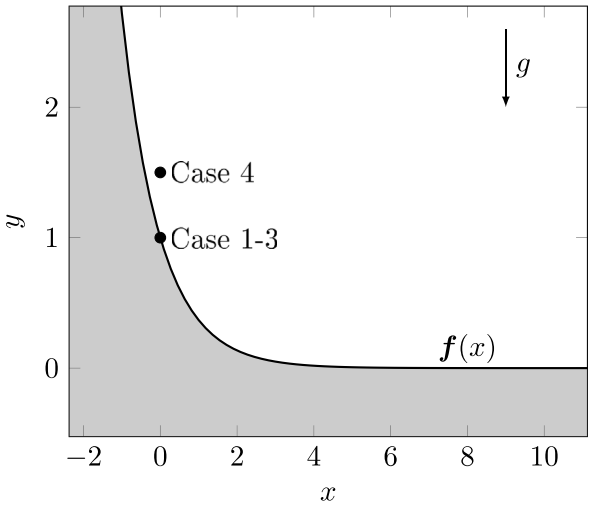

Fig. 6. Sketch of the point mass falling and sliding on a slope.

5.3. Point mass on slope

In order to investigate the order of convergence of the proposed method we consider a point mass (mass $m = \pi$, gravity constant $g = 10$) falling and sliding on a slope described by an exponential function, see Fig. 6. Let the Cartesian position coordinates of the mass be $\boldsymbol{q} = (x,\ y)$ and the generalized velocities $\boldsymbol{u} = \dot{\boldsymbol{q}} = (u_x,\ u_y)$. Consequently,

$$\boldsymbol{M} = \operatorname{diag}(m,\ m) \quad \text{and} \quad \boldsymbol{h} = (0,\ -mg)\,. \tag{50}$$

The curve $\boldsymbol{f} : \mathbb{R} \to \mathbb{R}^2$, defining the slope, and its first derivative are given by

$$\boldsymbol{f}(x) = \big(x,\ \exp(-x)\big)\,, \quad \boldsymbol{f}'(x) = \big(1,\ -\exp(-x)\big)\,, \tag{51}$$

see Fig. 6. Hence, we can compute the tangent and normal of a possible contact as

$$\boldsymbol{t}(x) = \frac{\boldsymbol{f}'(x)}{\|\boldsymbol{f}'(x)\|}\,, \quad \boldsymbol{n}(x) = \begin{pmatrix} 0 & -1 \\ 1 & 0 \end{pmatrix} \boldsymbol{t}(x)\,. \tag{52}$$

Consequently, the normal contact distance and relative tangential velocity are given by

$$g_N(\boldsymbol{q}) = \boldsymbol{n}(x)^{\mathrm{T}}\big(\boldsymbol{q} - \boldsymbol{f}(x)\big) \quad \text{and} \quad \gamma_F(\boldsymbol{q}, \boldsymbol{u}) = \boldsymbol{t}(x)^{\mathrm{T}}\boldsymbol{u}\,. \tag{53}$$

Assuming inelastic impacts, the description is completed by the parameters $e_N = e_F = 0$ and $\mu = 0.3$. Constraint derivatives and generalized force directions for the unilateral constrains are obtained by differentiation of (53) with respect to time t and generalized velocities $\boldsymbol{u}$, respectively. Depending on the chosen initial conditions four scenarios were studied.

Case 1:. Let $t_0 = 0$, $x_0 = x(t_0) = 0$ and $\boldsymbol{q}_0 = \boldsymbol{q}(t_0) = \boldsymbol{f}(x_0) = (0,\ 1)$. Hence, the point mass lies on the slope. For $\boldsymbol{u}_0 = \boldsymbol{u}(t_0) = (0,\ 0)$ the mass starts at rest with $\gamma_F(t_0) = 0$. The initial accelerations $\dot{\boldsymbol{u}}_0 = \dot{\boldsymbol{u}}(t_0)$ and constraint forces $\lambda_{N,0} = \lambda_N(t_0)$, $\lambda_{F,0} = \lambda_F(t_0)$ have to satisfy

$$\ddot{g}_N(t_0, \boldsymbol{q}_0, \boldsymbol{u}_0, \dot{\boldsymbol{u}}_0) \in \mathcal{N}_{\mathbb{R}_0^-}(-\lambda_{N,0}) \quad \text{and} \quad \dot{\gamma}_F(t_0, \boldsymbol{q}_0, \boldsymbol{u}_0, \dot{\boldsymbol{u}}_0) \in \mathcal{N}_{C_F(\lambda_{N,0})}(-\lambda_{F,0})\,. \tag{54}$$

This can be understood as Signorini's law (8) and Coulomb's friction law (16) formulated on acceleration level, see Chapter 7 in Ref. [4].

Case 2:. Starting on the slope as above, but with a nonzero initial velocity with $u_0 = 1$ and $\boldsymbol{u}_0 = \boldsymbol{t}(x_0)u_0$, the point mass starts in slip with $\gamma_F(t_0) \neq 0$. In this case, assuming Coulomb's friction law, the initial accelerations and constraint forces are determined by

$$\ddot{g}_N(t_0, \boldsymbol{q}_0, \boldsymbol{u}_0, \dot{\boldsymbol{u}}_0) \in \mathcal{N}_{\mathbb{R}_0^-}(-\lambda_{N,0}) \quad \text{and} \quad \lambda_{F,0} = -\mu\lambda_{N,0}\frac{\gamma_F(t_0, \boldsymbol{q}_0, \boldsymbol{u}_0)}{\|\gamma_F(t_0, \boldsymbol{q}_0, \boldsymbol{u}_0)\|}\,. \tag{55}$$

Case 3:. Case 2 with $u_0 = -1$.

Case 4:. Starting above the slope with $\boldsymbol{q}_0 = (0,\ 1.5)$ and $\boldsymbol{u}_0 = (0,\ 0)$. A single inelastic impact occurs and the point mass starts sliding on the slope until stick.

The trajectories of Cases 1 to 4 are illustrated in Fig. 7. In Cases 1 and 2, the trajectories exhibit smooth curves until stick is reached. However, a notable contrast is observed in Case 3, where a backward-forward slip transition occurs after a short time

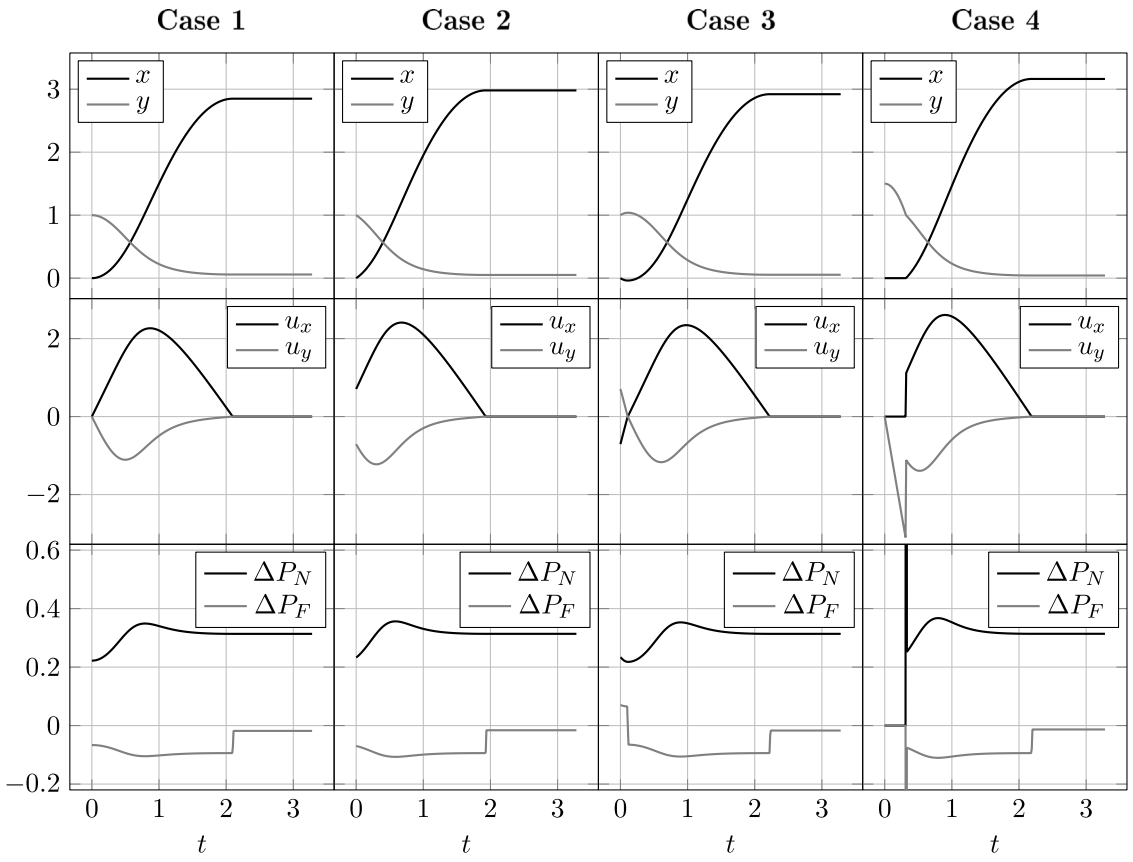

Fig. 7. Exemplary results of the point mass on slope example for Case 1 to 4.

interval, resulting in a kink in velocities and discontinuous percussion increments. In the final case, the starting position is situated above the slope, leading to a single inelastic impact that introduces discontinuous velocities and percussion increments. It is worth noting that in all cases, the ultimate slip-stick transition manifests as a velocity kink and a discontinuity in percussion increments.

To investigate the convergence properties of the proposed method, simulations were performed for different step-sizes. Using a semismooth Newton method, the nonlinear equations (41) and (43) where solved up to an absolute error of 10^{-12} with the proximal point parameters $r_N = r_F = 0.1$. A reference solution was computed with a step-size $\Delta t = 5 \cdot 10^{-5}$ until a final time $t_{\text{final}} = 2^{16}\Delta t = 3.2768$ was reached. All other solutions were computed with $\Delta t \in \{2 \cdot 10^{-4},\ 4 \cdot 10^{-4},\ 8 \cdot 10^{-4},\ 1.6 \cdot 10^{-3},\ 3.2 \cdot 10^{-3},\ 6.4 \cdot 10^{-3},\ 1.28 \cdot 10^{-2},\ 2.56 \cdot 10^{-2}\}$. Since these step-sizes are multiples of the reference step-size, the resulting discrete time grids always share the grid points of the coarser mesh. For the discrete time instants $t_1, t_2, \dots, t_N$ we introduce the discrete function values $\boldsymbol{f} = (f_1, f_2, \dots, f_N)$ and their corresponding values of the reference solution $\bar{\boldsymbol{f}} = (\bar{f}_1, \bar{f}_2, \dots, \bar{f}_N)$. Hence, we follow [15] and introduce the error measure

$$\|\boldsymbol{f} - \bar{\boldsymbol{f}}\|_p = \left(\Delta t \sum_{i=1}^{N} |f_i - \bar{f}_i|^p \right)^{\frac{1}{p}}, \quad 1 \le p < \infty, \quad i = 1, 2, \dots, N. \tag{56}$$

Since $\|\boldsymbol{f} - \bar{\boldsymbol{f}}\|_1 \ge \|\boldsymbol{f} - \bar{\boldsymbol{f}}\|_p$, we subsequently restrict ourselves to the former one. For vector valued quantities, we used the maximum $\|\boldsymbol{f} - \bar{\boldsymbol{f}}\|_1$ error over all components. Hence, we investigated the errors $e_q = \max\{\|\boldsymbol{x} - \bar{\boldsymbol{x}}\|_1, \|\boldsymbol{y} - \bar{\boldsymbol{y}}\|_1\}$, $e_u = \max\{\|\boldsymbol{u}_x - \bar{\boldsymbol{u}}_x\|_1, \|\boldsymbol{u}_y - \bar{\boldsymbol{u}}_y\|_1\}$, $e_{\Delta P_N} = \|\Delta \boldsymbol{P}_N - \Delta \bar{\boldsymbol{P}}_N\|_1$ and $e_{\Delta P_F} = \|\Delta \boldsymbol{P}_F - \Delta \bar{\boldsymbol{P}}_F\|_1$.

The convergence behavior of all four cases is depicted in Fig. 8. It can readily be seen, that in the first two cases the generalized positions and velocities are solved with second-order accuracy, although the solution involves a slip-stick transition. This is an expected result since in the case of persistent frictional contact (without changing contact status, i.e., no slip-stick transition or forward–backward/ backward-forward slip transition) the problem can be described by an index 3 DAE. For such problems the classical RATTLE algorithm can be shown to be second-order accurate [30]. In contrast, the percussion increments indicate first-order convergence. If an equivalently accurate approximation of the Lagrange multipliers is required, their values can be computed a posteriori using the constraint equations on acceleration level [30]. However, such an accuracy is often unnecessary and involves the cumbersome derivation of extra constraint derivatives, cf. [18,19,23]. In Case 3 and 4 an order reduction is observed and the generalized positions and velocities indicate a non-monotone convergence of order one. For problems with discontinuous velocities (e.g. Case 4) this observation is in line with the findings of [25] within a related problem.

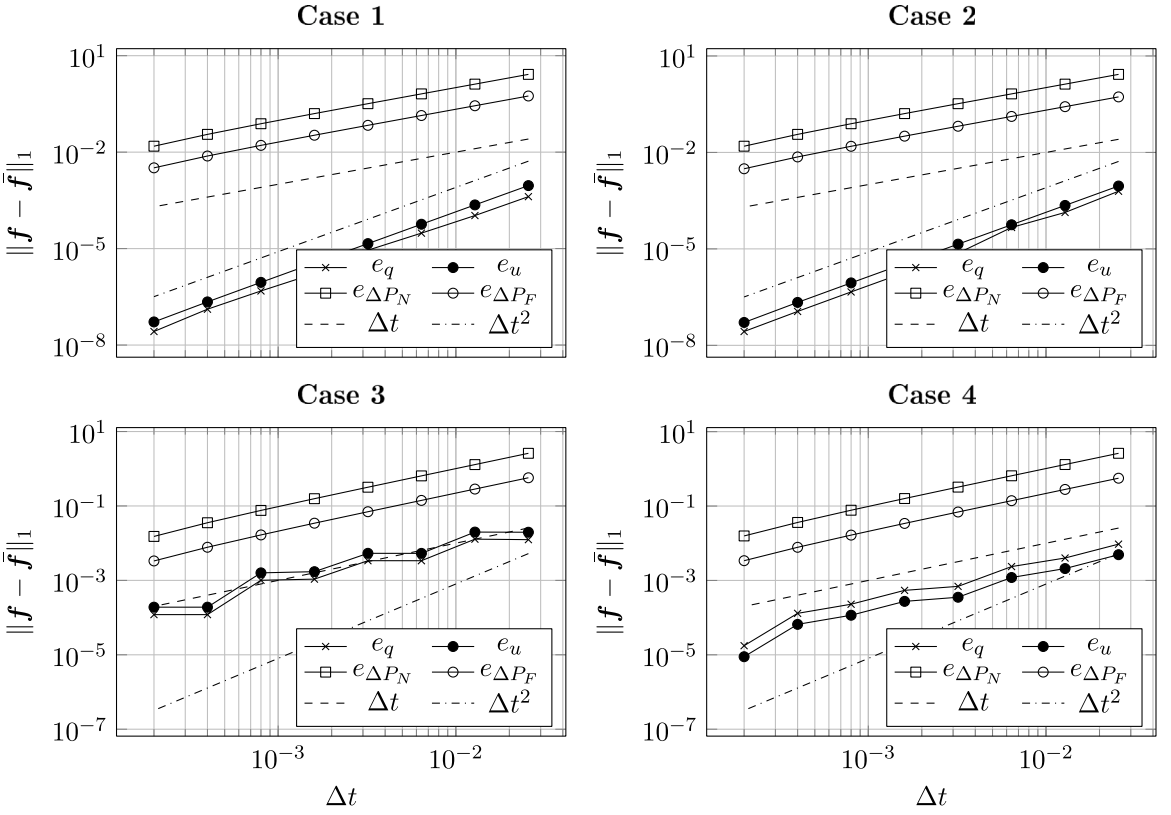

Fig. 8. Convergence behavior Case 1 to 4.

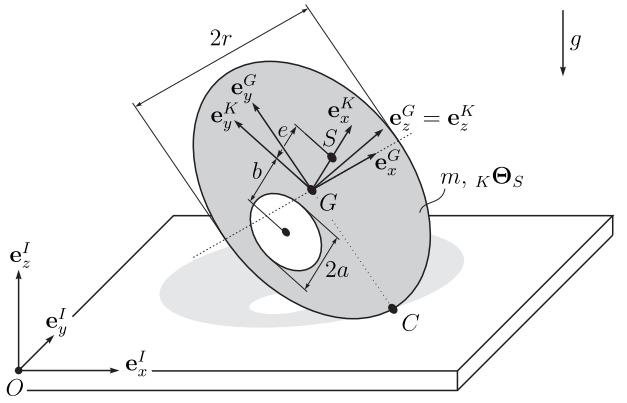

Fig. 9. Sketch of the Tippedisk.

5.4. Tippedisk

The tippedisk — a tippetop without rotational symmetry is an important mechanical-mathematical archetype for friction-induced instability phenomena [45]. Furthermore, it serves as an excellent benchmark example for the validation of nonsmooth solution algorithms. Essentially, the tippedisk is an eccentric disk of mass $m = 0.435$, whose center of gravity S does not coincide with the geometric center G of the disk, see Fig. 9. One way to construct such a tippedisk is to take a homogeneous disk of radius $r = 4.5 \cdot 10^{-2}$ and remove mass at the distance $b = 2 \cdot 10^{-2}$ by drilling a hole of radius $a = 1.5 \cdot 10^{-2}$. The eccentricity e then follows as $e = ba^2/(r^2 - a^2)$. Consequently, the inertia matrix is ${}_K\boldsymbol{\Theta}_S = \mathrm{diag}(2.49 \cdot 10^{-4},\ 2.2972 \cdot 10^{-4},\ 4.7072 \cdot 10^{-4})$. If such a specimen is placed on a flat support, like a flat table, in the gravitational field with $g = 9.81$, it is quite obvious that there are two stationary spinning solutions where the gravitational force and the normal contact force balance each other. Namely, a solution where the center of

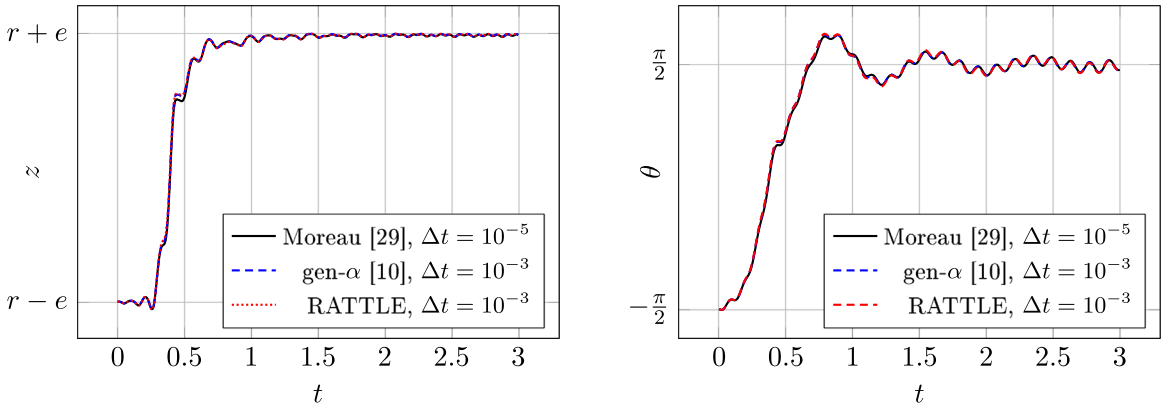

Fig. 10. Simulation results Tippedisk: Simulated time evolution of the center of mass z (left) and inclination angle θ corresponding to the last Euler angle with sequence "zxz" (right). Solid black: Moreau's time-stepping method [36], dashed blue: Nonsmooth generalized-alpha method [18], dotted red: presented method.

gravity S is below the geometric center G and one where S is vertically above G. We refer to former one as *non-inverted solution*, while the ladder one is called *inverted solution*. If the non-inverted tippedisk is spun fast around an in-plane axis, the center of gravity rises until the disk ends in an inverted configuration, which is called the inversion phenomenon. However, due to dissipation, the spinning velocity decreases slowly over time.

We describe the position of the disk by the components ${}_I\boldsymbol{r}_{OS} \in \mathbb{R}^3$ of the position vector of S with respect to the inertial basis I. To characterize the orientation of the disk, we introduce the body fixed K-basis such that $\boldsymbol{e}_z^K$ is the normal with respect to the face of the disk. The transformation matrix $\boldsymbol{A}_{IK} = ({}_I\boldsymbol{e}_x^K \ {}_I\boldsymbol{e}_y^K \ {}_I\boldsymbol{e}_z^K)$ is parametrized using a unit quaternion $\boldsymbol{p} \in \mathbb{R}^4$. Hence, the configuration of the disk is described by $\boldsymbol{q} = ({}_I\boldsymbol{r}_{OS}, \ \boldsymbol{p}) \in \mathbb{R}^7$. The generalized velocities are $\boldsymbol{u} = ({}_I\boldsymbol{v}_S, \ {}_K\boldsymbol{\omega}_{IK}) \in \mathbb{R}^6$ composed of the representations of the velocity $\boldsymbol{v}_S$ of the center of mass S and the angular velocity $\boldsymbol{\omega}_{IK}$ of the K-basis with respect to the I and K-basis, respectively. As mentioned in Section 2, this choice leads to a model with the generalized kinematic equation (1). For the relevant quantities $\boldsymbol{B}$, $\boldsymbol{\beta}$, $\boldsymbol{M}$, and $\boldsymbol{h}$ describing such a parametrized rigid body under the influence of gravity, we refer to model 4 in [45].

The contact distance between the disk and the flat support is described by

$$g_N = \boldsymbol{r}_{OC} \cdot \boldsymbol{e}_z^I = (\boldsymbol{r}_{OS} + \boldsymbol{r}_{SC}) \cdot \boldsymbol{e}_z^I \,. \tag{57}$$

Following [45], we can introduce the grinding G-basis as

$$\boldsymbol{e}_z^G = \boldsymbol{e}_z^K \,, \quad \boldsymbol{e}_x^G = \frac{\boldsymbol{e}_z^I \times \boldsymbol{e}_z^G}{\|\boldsymbol{e}_z^I \times \boldsymbol{e}_z^G\|} \,, \quad \boldsymbol{e}_y^G = \boldsymbol{e}_z^G \times \boldsymbol{e}_x^G \tag{58}$$

and conclude $\boldsymbol{r}_{SC} = -e\boldsymbol{e}_x^K - r\boldsymbol{e}_y^G$, see Fig. 9. As discussed in [45], pure Coulomb friction is not sufficient to describe the experimentally observed inversion phenomenon. Hence, an approximation of set-valued Coulomb–Contensou friction is taken into account by using the set transformations introduced in [36] with radius of assumed circular contact area $R = 10^{-3}$. To this end, we use the contact velocities

$$\boldsymbol{\gamma}_F = \begin{pmatrix} \boldsymbol{v}_C \cdot \boldsymbol{e}_x^I \\ \boldsymbol{v}_C \cdot \boldsymbol{e}_y^I \\ \frac{3\pi R}{16} \boldsymbol{\omega}_{IK} \cdot \boldsymbol{e}_z^I \end{pmatrix}, \tag{59}$$

where $\boldsymbol{v}_C = \boldsymbol{v}_S + \boldsymbol{\omega}_{IK} \times \boldsymbol{r}_{SC}$ denotes the velocity of the contact point. A closer look at the contact velocities (59) reveals that the first two components correspond to tangential contact velocities and capture isotropic Coulomb friction. Moreover, the third component is a representative radial contact velocity, which accounts for drilling friction.

The initial conditions were taken as $t_0 = 0$, ${}_I\boldsymbol{r}_{OS}(t_0) = (0, \ 0, \ r - e)$, $\boldsymbol{p}(t_0) = (0.5, \ 0.5, \ 0.5, \ -0.5)$, ${}_K\boldsymbol{\omega}_{IK}(t_0) = (-60, \ 0, \ 1)$ and ${}_I\boldsymbol{v}_S(t_0) = \left(\boldsymbol{A}_{IK}(\boldsymbol{p}(t_0))_K\boldsymbol{\omega}_{IK}(t_0)\right) \times {}_I\boldsymbol{r}_{OS}(t_0)$. The simulations were performed using a constant step-size $\Delta t = 10^{-3}$ and the proximal point parameters $r_N = r_F = 0.1$. Using a semismooth Newton method, the nonlinear equations (41) and (43) where solved up to an absolute error of 10^{-8}. For comparison, we have also solved the system with a variant of Moreau's time-stepping method [36] and the nonsmooth generalized-alpha method of [18]. Since the former one does not prevent penetration, a very small step-size of $\Delta t = 10^{-5}$ has to be chosen in order to accurately represent the observed inversion phenomenon. For the second-order method of [18], we chose the same step-size as for the nonsmooth RATTLE method, i.e., $\Delta t = 10^{-3}$, and $\rho_\infty = 0.9$.

It is apparent from Fig. 10 that the simulation results using the presented algorithm are in line with the results obtained with the method of [36], although a hundred times larger step-size was used. This shows that the presented method is well suited for mechanical systems with spatial friction as well as models with a general kinematic differential equation (1). Since a significantly

larger step-size was used, the number of required operations was reduced, resulting in substantial cost savings for the overall computation. Moreover, the results are in line with those computed with the method presented in [18]. Hence, for persistent frictional contact, the second-order convergence of the presented method is of crucial importance for the efficient solution of highly dynamic problems like the tippedisk.

6. Conclusion

Higher-order time integration methods provide improved accuracy and computational efficiency. They lead to more precise simulation results, while simultaneously reducing computational costs due to possible larger step-sizes. These are only a few arguments to seek for higher-order methods for solving mechanical systems subjected to bilateral and unilateral constraints. The extension of existing, well-established higher-order methods is not straightforward. Although some attempts were made, they either suffer from penetration problems, involve complex contact formulation on all three kinematic levels (position, velocity and acceleration) or collapse to a first-order method for persistent frictional contact, even in cases with constant sliding state (e.g. no slip-stick transition).

The RATTLE algorithm is a well-established second-order accurate method for the solution of constrained mechanical systems and enforces the constraints to be satisfied on position and velocity level. In this paper the method is extended to cope with unilateral constraints and friction. Moreover, normal and tangent impacts are included and at the same time (bilateral) constraint drift or contact penetration is prohibited.

Selected numerical examples showcase the versatility and robustness of the proposed method in various applications. The method can overcome accumulation points (Zeno phenomenon), correctly handles slip-stick transitions, copes with nontrivial kinematic relations and impressively yields second-order accurate positions and velocities in phases where the contact status does not change (i.e. no collisions/constant sliding states).

CRediT authorship contribution statement

Jonas Breuling: Conceptualization, Methodology, Formal analysis, Software, Writing – original draft. **Giuseppe Capobianco:** Conceptualization, Methodology, Formal analysis, Software, Writing – review & editing. **Simon R. Eugster:** Conceptualization, Writing – review & editing, Supervision. **Remco I. Leine:** Conceptualization, Writing – review & editing, Supervision.

Declaration of competing interest

The authors declare that they have no known competing financial interests or personal relationships that could have appeared to influence the work reported in this paper.

Data availability

Data will be made available on request.

References

[1] J.J. Moreau, Unilateral contact and dry friction in finite freedom dynamics, in: J.J. Moreau, P.D. Panagiotopoulos (Eds.), Non-Smooth Mechanics and Applications. CISM Courses and Lectures, Springer, Wien, 1988, pp. 1–82.
[2] B. Brogliato, Nonsmooth Mechanics: Models, Dynamics and Control, in: Communications and Control Engineering, Springer International Publishing, 2016.
[3] V. Acary, B. Brogliato, in: F. Pfeiffer, P. Wrigger (Eds.), Numerical Methods for Nonsmooth Dynamical Systems: Applications in Mechanics and Electronics, in: Lecture Notes in Applied and Computational Mechanics, vol. 35, Springer, Berlin, Heidelberg, 2008.
[4] C. Glocker, Set-Valued Force Laws, Springer, Berlin, Heidelberg, 2001.
[5] R.I. Leine, H. Nijmeijer, Dynamics and Bifurcations of Non-Smooth Mechanical Systems, in: Lecture Notes in Applied and Computational Mechanics, vol. 18, Springer, Berlin, Heidelberg, 2004.
[6] C. Glocker, E. Cataldi-Spinola, R. Leine, Curve squealing of trains: Measurement, modelling and simulation, J. Sound Vib. 324 (1) (2009) 365–386.
[7] R.I. Leine, A. Schweizer, M. Christen, J. Glover, P. Bartelt, W. Gerber, Simulation of rockfall trajectories with consideration of rock shape, Multibody Syst. Dyn. 32 (2) (2014) 241–271.
[8] D.E. Stewart, J.C. Trinkle, An implicit time-stepping scheme for rigid body dynamics with inelastic collisions and coulomb friction, Internat. J. Numer. Methods Engrg. 39 (15) (1996) 2673–2691.
[9] M. Jean, J.J. Moreau, Unilaterality and dry friction in the dynamics of rigid body collections, in: 1st Contact Mechanics International Symposium, Lausanne, Switzerland, 1992, pp. 31–48.
[10] J.J. Moreau, Numerical aspects of the sweeping process, Comput. Methods Appl. Mech. Engrg. 177 (1999) 329–349.
[11] M. Jean, The non-smooth contact dynamics method, Comput. Methods Appl. Mech. Engrg. 177 (3) (1999) 235–257.
[12] L. Paoli, M. Schatzman, A numerical scheme for impact problems I: The one-dimensional case, SIAM J. Numer. Anal. 40 (2) (2002) 702–733.
[13] L. Paoli, M. Schatzman, A numerical scheme for impact problems II: The multidimensional case, SIAM J. Numer. Anal. 40 (2) (2002) 734–768.
[14] C. Studer, R.I. Leine, C. Glocker, Step size adjustment and extrapolation for time-stepping schemes in non-smooth dynamics, Internat. J. Numer. Methods Engrg. 76 (11) (2008) 1747–1781.
[15] V. Acary, Higher order event capturing time-stepping schemes for nonsmooth multibody systems with unilateral constraints and impacts, Appl. Numer. Math. 62 (10) (2012) 1259–1275, Selected Papers from NUMDIFF-12.
[16] T. Schindler, V. Acary, Timestepping schemes for nonsmooth dynamics based on discontinuous Galerkin methods: Definition and outlook, Math. Comput. Simulation 95 (2014) 180–199, Discontinuous Differential Systems : Theory and Numerical Methods.

[17] Q.-Z. Chen, V. Acary, G. Virlez, O. Brüls, A nonsmooth generalized-α scheme for flexible multibody systems with unilateral constraints, Internat. J. Numer. Methods Engrg. 96 (8) (2013) 487–511.
[18] G. Capobianco, J. Harsch, S.R. Eugster, R.I. Leine, A nonsmooth generalized-alpha method for mechanical systems with frictional contact, Internat. J. Numer. Methods Engrg. 122 (22) (2021) 6497–6526.
[19] O. Brüls, V. Acary, A. Cardona, Simultaneous enforcement of constraints at position and velocity levels in the nonsmooth generalized-α scheme, Comput. Methods Appl. Mech. Engrg. 281 (2014) 131–161.
[20] C.W. Gear, B. Leimkuhler, G.K. Gupta, Automatic integration of Euler-Lagrange equations with constraints, J. Comput. Appl. Math. 12 (1985) 77–90.
[21] V. Acary, Projected event-capturing time-stepping schemes for nonsmooth mechanical systems with unilateral contact and Coulomb's friction, Comput. Methods Appl. Mech. Engrg. 256 (2013) 224–250.
[22] S. Schoeder, H. Ulbrich, T. Schindler, Discussion of the Gear–Gupta–Leimkuhler method for impacting mechanical systems, Multibody Syst. Dyn. 31 (4) (2014) 477–495.
[23] O. Brüls, V. Acary, A. Cardona, On the constraints formulation in the nonsmooth generalized-α method, in: Advanced Topics in Nonsmooth Dynamics, Springer, 2018, pp. 335–374.
[24] A. Cosimo, J. Galvez, F.J. Cavalieri, A. Cardona, O. Brüls, A robust nonsmooth generalized-α scheme for flexible systems with impacts, Multibody Syst. Dyn. 48 (2) (2020) 127–149.
[25] J. Galvez, F.J. Cavalieri, A. Cosimo, O. Brüls, A. Cardona, A nonsmooth frictional contact formulation for multibody system dynamics, Internat. J. Numer. Methods Engrg. 121 (16) (2020) 3584–3609.
[26] A. Cosimo, F.J. Cavalieri, J. Galvez, A. Cardona, O. Brüls, A general purpose formulation for nonsmooth dynamics with finite rotations: Application to the woodpecker toy, J. Comput. Nonlinear Dyn. 16 (3) (2021).
[27] E. Hairer, C. Lubich, G. Wanner, Geometric Numerical Integration: Structure-Preserving Algorithms for Ordinary Differential Equations, second ed., in: Springer Series in Computational Mathematics, (31) Springer, Berlin, New York, 2006.
[28] J.-P. Ryckaert, G. Ciccotti, H.J. Berendsen, Numerical integration of the cartesian equations of motion of a system with constraints: molecular dynamics of n-alkanes, J. Comput. Phys. 23 (3) (1977) 327–341.
[29] H.C. Andersen, Rattle: A "velocity" version of the shake algorithm for molecular dynamics calculations, J. Comput. Phys. 52 (1) (1983) 24–34.
[30] L. Jay, Symplectic partitioned Runge–Kutta methods for constrained Hamiltonian systems, SIAM J. Numer. Anal. 33 (1) (1996) 368–387.
[31] S. Hante, M. Arnold, RATTLie: A variational Lie group integration scheme for constrained mechanical systems, J. Comput. Appl. Math. 387 (2021) 112492.
[32] J. Kleinert, B. Simeon, K. Dreßler, Nonsmooth Contact Dynamics for the large-scale simulation of granular material, J. Comput. Appl. Math. 316 (2017) 345–357, Selected Papers from NUMDIFF-14.
[33] B.J. Leimkuhler, R.D. Skeel, Symplectic Numerical Integrators in Constrained Hamiltonian Systems", J. Comput. Phys. 112 (1) (1994) 117–125.
[34] R.I. Leine, N. van de Wouw, Stability and Convergence of Mechanical Systems with Unilateral Constraints, Lecture Notes in Applied and Computational Mechanics, vol. 36, Springer-Verlag, Berlin, 2008.
[35] C. Glocker, Simulation of hard contacts with friction: an iterative projection method, in: Recent Trends in Dynamical Systems, Springer, 2013, pp. 493–515.
[36] M. Möller, R.I. Leine, C. Glocker, An efficient approximation of orthotropic set-valued force laws of normal cone type, in: 7th Euromech Solid Mechanics Conference, Lisbon, 2009, pp. 7–11.
[37] T. Winandy, M. Baumann, R.I. Leine, Variational analysis of inequality impact laws for perfect unilateral constraints, in: Advanced Topics in Nonsmooth Dynamics, Springer, 2018, pp. 47–92.
[38] P. Alart, A. Curnier, A mixed formulation for frictional contact problems prone to Newton like solution methods, Comput. Methods Appl. Mech. Engrg. 92 (1991) 353–375.
[39] V. Acary, M. Brémond, O. Huber, On solving contact problems with Coulomb friction: formulations and numerical comparisons, in: Advanced Topics in Nonsmooth Dynamics, Springer, 2018, pp. 375–457.
[40] M. Hintermüller, K. Ito, K. Kunisch, The primal-dual active set strategy as a semismooth Newton method, SIAM J. Optim. 13 (3) (2002) 865–888.
[41] M. Wösle, F. Pfeiffer, Dynamics of multibody systems containing dependent unilateral constraints with friction, J. Vib. Control 2 (2) (1996) 161–192.
[42] C. Studer, in: F. Pfeiffer, P. Wriggers (Eds.), Numerics of Unilateral Contacts and Friction: Modeling and Numerical Time Integration in Non-Smooth Dynamics, in: Lecture Notes in Applied and Computational Mechanics, vol. 47, Springer, Berlin, Heidelberg, 2009.
[43] C. Glocker, Dynamik von Starrkörpersystemen mit Reibung und Stößen (Ph.D. thesis), TU München, 1995.
[44] P. Flores, R. Leine, C. Glocker, Modeling and analysis of planar rigid multibody systems with translational clearance joints based on the non-smooth dynamics approach, Multibody Syst. Dyn. 23 (2) (2010) 165–190.
[45] S. Sailer, S.R. Eugster, R.I. Leine, The tippedisk: a tippetop without rotational symmetry, Regul. Chaotic Dyn. 25 (6) (2020) 553–580.